Computers and Mathematics with Applications 148 (2023) 26–40

Contents lists available at ScienceDirect

Computers and Mathematics with Applications

journal homepage: www.elsevier.com/locate/camwa

Tent-pitcher spacetime discontinuous Galerkin method for one-dimensional linear hyperbolic and parabolic PDEs

Giang D. Huynh *, Reza Abedi

The University of Tennessee Knoxville (UTK), Space Institute (UTSI), United States of America

ARTICLE INFO

Keywords:
Discontinuous Galerkin
Spacetime
Parabolic
Transfer matrix
Spectral stability

ABSTRACT

We present a spacetime DG method for 1D spatial domains and three linear hyperbolic, damped hyperbolic, and parabolic PDEs. The latter two correspond to Maxwell-Cattaneo-Vernotte (MCV) and Fourier heat conduction problems. The method is called the tent-pitcher spacetime DG method (tpSDG) due to its resemblance to the causal spacetime DG method (cSDG) wherein the solution advances in time by pitching spacetime patches. The tpSDG method extends the applicability of such methods from hyperbolic to parabolic and hyperbolic PDEs. For problems with a spatially uniform mesh, a transfer matrix approach is derived wherein the inflow, boundary, and source term values are mapped to the solution coefficient and output values. This resembles a finite difference scheme, but with grid points at the Gauss points of the spatial elements and arbitrarily tunable order of accuracy in spacetime. The spectral stability analysis of the method provides stability correction factors for the parabolic case. Numerical examples demonstrate the applicability of the method to problems with heterogeneous material properties.

1. Introduction

Discontinuous Galerkin (DG) methods have several advantages over (continuous) *Finite Element Methods* (FEMs) including element-level satisfaction of balance laws, exceptional flexibility in *h*-, *p*-, and *hp*-adaptive operations, and more compact element communication stencil that lends itself to better parallel computing. Moreover, when an explicit time integrator is used for transient problems, their block diagonal mass matrix directly leads to an element-by-element solution process. Finally, their discontinuous solution nature is suitable for hyperbolic *Partial Differential Equations* (PDEs) where discontinuities and shocks persist or are generated mid simulation for nonlinear PDEs. Consequently, DG methods are widely used for the solution of parabolic and especially hyperbolic PDEs. We refer the reader to [1–5] for further discussion on these aspects.

Four desirable features pertained to temporal advance of the solution for transient PDEs are discussed and referred to in the remainder of this section. First, the temporal order of accuracy is easily tunable to high values. Second, ideally there is the flexibility to adjust such order at the element level, as opposed to the entire spatial domain. Third, the time advance is adjustable for individual elements, as opposed to taking a globally uniform time advance. Fourth, these aspects, *i.e.*, temporal order and step size, and the spatial mesh layout can change as solution features and wave fronts travel in the spacetime domain. Features three and four can be viewed as local *h*- and *p*-adaptivity in time.

There are several approaches to achieve these desirable features. First, a *Spacetime Discontinuous Galerkin* (SDG) method often refers to a discretization where the space domain is extruded in time, with the possibility of some nodal perturbation, to form spacetime elements [6–13]. Since the solution is directly interpolated in spacetime, the first two features are easily achieved with SDG methods. In their adaptive versions [14], the latter two features can be achieved too. Second, some space DG methods use the *Cauchy-Kovalewski* (CK) or *Lax-Wendroff* procedure to achieve arbitrarily high orders of accuracy in time as in [15] and *arbitrary high-order derivatives* (ADER) DG methods [16–19]. This achieves feature one, and in fact in versions of these methods with *Local Time Stepping* (LTS) option features two and three are achieved. Specifically, pertained to feature three, each element can achieve its maximum stable time advance which is quite impressive. However, we note that the CK approach becomes quite challenging for nonlinear PDEs [19]. Third, there is a group of spacetime DG methods for hyperbolic PDEs, wherein the boundaries of elements (or groups of elements called *patches*) are *causal* resulting in a local solution process, capable of achieving all the

* Corresponding author.
E-mail address: ghuynh1@vols.utk.edu (G.D. Huynh).

https://doi.org/10.1016/j.camwa.2023.07.021
Received 20 December 2022; Received in revised form 16 May 2023; Accepted 22 July 2023
Available online 16 August 2023

four features above. These methods, referred to as *causal SDG* (cSDG) from hereon, will be discussed next.

The cSDG methods were first presented for 1D hyperbolic PDEs in [20,21]. The *Tent-Pitcher* algorithm [22,23] advances the solution by erecting a patch of elements around vertices with local time coordinate for 2D and 3D problems. Similar to the SDG methods, direct discretization of spacetime achieves features one and two above. Feature three is very naturally achieved as the time advance of each patch is only based on the geometry and element sizes of the patch. As will be discussed in §4.2, this time advance is optimal and superior to that of the ADER DG methods mentioned above. Finally, mesh adaptive operations in [23,24] achieve feature four. In fact, the richer vocabulary of spacetime meshing operations makes it feasible to track complex moving interfaces such as crack surfaces in spacetime [25,26]. Its due to these unique features that various novel integration schemes and Trefftz methods are proposed in [27–32].

This work extends prior works in two respects. First, all cSDG methods are formulated for hyperbolic PDEs. Herein, we present the so-called *Tent-Pitching SDG* (tpSDG) method that not only applies to hyperbolic PDEs, but also extends to parabolic PDEs, with the potential of achieving most or all of the features discussed above even for parabolic PDEs. Second, a particular implementation for 1D case is considered, where the spacetime meshing starts from a spatial grid with uniform element size. This provides a quadrature-free solution advance method using transfer matrices that map *Initial Conditions* (ICs) / predecessor element solutions, *Boundary Conditions* (BCs), and source terms to the outflow facets of patches. This is motivated by the derivation of finite difference schemes from low order discontinuous Galerkin methods as discussed in [27,33], with the difference that herein the grid points are the Gauss points of interiors and facets of spacetime elements and the order of accuracy in spacetime is easily tunable.

The outline of the paper is as follows. The DG formulation for three hyperbolic and parabolic linear PDEs for heat conduction and wave equation is presented in §2, followed by the derivation and implementation of the transfer matrix method for uniform 1D grids in §3. The stable time advance limits for hyperbolic and parabolic cases are obtained in §4. The importance of extension of SDG method to dH and P PDEs and extension of the transfer matrix approach to 2D and 3D problems is discussed in §5. Convergence studies and a few numerical results are presented in §6, before drawing the final conclusions in §7.

2. Formulation

We present the formulation for the tpSDG method for a 1D and linear hyperbolic or parabolic PDE. The patch-level formulation of the weak statement results in the proposed quadrature-free transfer matrix approach.

2.1. Governing equations

Motivated by the 1D heat conduction problem, consider the following system of equations,

$$CT_{,t} + q_{,x} = Q \tag{1a}$$

$$\tau q_{,t} + \kappa T_{,x} = -\eta q, \tag{1b}$$

where T is temperature, q heat flux, Q heat source, C volumetric heat capacity, τ relaxation time and κ heat conductivity. Equation (1a) is the strong form of balance of energy and (1b) is the constitutive equation for heat flux q.

The three cases of the PDE correspond to different forms of (1b) and are summarized in Table 1. First, if $\eta = 1$ and $\tau = 0$, (1b) corresponds to the classical Fourier heat conduction model, and the system of equations (1) is the parabolic heat conduction model, expressed as $CT_{,t} - (\kappa T_{,x})_{,x} = Q$ in terms of the temperature field only. Second, if the relaxation time is positive ($\tau > 0$) and $\eta = 1$, heat flux cannot simply obtained from the temperature and requires the solution of the differential equation (1b). The system of equations (1) is called the Maxwell-Cattaneo-Vernotte (MCV) heat conduction equations after [34,35]. Expressed in terms of temperature, the MCV equation is $\tau CT_{,tt} + CT_{,t} - (\kappa T_{,x})_{,x} = Q + \tau Q_{,t}$ [36]. This is a hyperbolic PDE with a wave speed of $c = \sqrt{\frac{\kappa}{\tau C}}$. It is one of several models that correctly capture the wave-like propagation of thermal energy at small space and time scales. Finally, the case $\tau > 0$, but $\eta = 0$ does not correspond to a heat model and is added to compare the solutions of the previous models with this undamped hyperbolic PDE, $\tau CT_{,tt} - (\kappa T_{,x})_{,x} = \tau Q_{,t}$. From hereon, these cases are labeled as *parabolic* (P), *damped hyperbolic* (dH), and *undamped hyperbolic* (H), respectively.

Table 1
The classification of PDEs corresponding to (1).

PDE and symbol	conditions	Example
Parabolic (P)	$\tau = 0, \eta = 1$	Fourier heat conduction
Damped hyperbolic (dH)	$\tau > 0, \eta = 1$	MCV
Undamped hyperbolic (H)	$\tau > 0, \eta = 0$	Wave equation

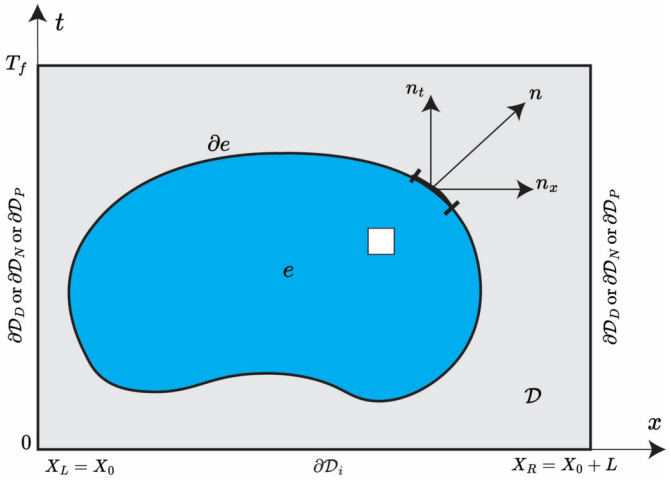

Fig. 1. Space-time domain $D \times [0, T_f]$ and an arbitrary volume e inside the domain.

The problem is considered for a 1D spatial domain $D = [X_L, X_R] = [X_0, X_0 + L]$ for the time interval $[0, T_f]$ as shown in Fig. 1. The *Initial Boundary Value Problem* (IBVP) includes the differential equations (1) and the following ICs and BCs,

$$T(x,0) = T_0(x), \qquad \text{on } \partial D_i \tag{2a}$$

$$q(x,0) = q_0(x), \qquad \text{on } \partial D_i \quad \text{(only for dH and H cases)} \tag{2b}$$

$$T(x,t) = \bar{T}(x,t), \qquad \text{on } \partial D_D \times [0, T_f], \tag{2c}$$

$$q_n(x,t) = q(x,t) n_x(x) = \bar{q}_n(x,t), \qquad \text{on } \partial D_N \times [0, T_f]. \tag{2d}$$

In addition to Dirichlet and Neumann BCs in (2c) and (2d), the *periodic boundary condition* (PBC) may be used on $\partial D_P = \{X_L, X_R\}$, where $T(X_R) = T(X_L)$ and $q(X_R) = q(X_L)$. These boundaries are mutually disjoint and satisfy $\partial D_D \cup \partial D_N \cup \partial D_P = \partial D = \{X_L, X_R\}$. The boundaries of the spacetime domain D are shown in Fig. 1.

2.2. Weak statement

The *Weighted Residual Statement* (WRS) is obtained by multiplying (1a) and $1/\kappa$ times of (1b) with temperature and heat flux weight functions $\hat{T}$ and $\hat{q}$, respectively, and integrating over an arbitrary spacetime domain e (see Fig. 1),

$$\int_e \Big(\hat{T}(CT_{,t}+q_{,x}-Q)+\hat{q}(\kappa^{-1}\tau q_{,t}+T_{,x}+\kappa^{-1}\eta q)\Big)\mathrm{d}V+$$
$$\int_{\partial e} \Big(\hat{T}\Big[(CT^*-CT)n_t+(q_n^*-qn_x)\Big]+ \tag{3}$$
$$\hat{q}\Big[\kappa^{-1}\tau(q^*-q)n_t+(T^*-T)n_x\Big]\Big)\mathrm{d}S=0,$$

where n_x and n_t are the spatial and temporal components of the spacetime normal vector as shown in the figure. The jump terms in the second line, are the corresponding jump terms of the differential equations in (1) and are expressed relative to T^* and q^*, the target values for temperature and heat flux, respectively. The integrals in the second line ensure weak enforcement of the jump conditions and continuity of the solution in this DG method. The target values are specified based on the ICs and BCs on the boundaries of the spacetime domain, and their values are provided in (6).

There are two comments about (3) and Fig. 1. First, in other cSDG formulations for various solid, fluid, thermal, and electromagnetics problems [36–40], the jump conditions and the PDEs are directly derived from the balance law statements in spacetime. Second, the definition of spacetime normal is problematic due to the lack of metric and dealing with length and time scales. In the aforementioned cSDG references, differential forms notation is used to address this challenge. However, such normal vectors are used in other DG methods that deal with slant interfaces in spacetime, see for example [6–8]. For brevity, we directly start with the PDEs (1) and do not resort to differential forms notation herein, but refer the reader to [38,40] for further details on these aspects.

After the application of the Gauss theorem on (3), the weak statement for the spacetime domain e is obtained as,

$$\int_e \Big(-\hat{T}_{,t}CT-\hat{T}_{,x}q-\hat{T}Q-\kappa^{-1}\tau\hat{q}_{,t}q-\hat{q}_{,x}T+\kappa^{-1}\eta\hat{q}q\Big)\mathrm{d}V+$$
$$\int_{\partial e}\Big(\hat{T}\Big[CT^*n_t+q_n^*\Big]+\hat{q}\Big[\kappa^{-1}\tau q^*n_t+T^*n_x\Big]\Big)\mathrm{d}S=0 \tag{4}$$

The solution (T,q) is sought for a broken Sobolev space corresponding to a partition of open spacetime domains $\{e_\alpha\}$ where the restriction of solution on each e in the partition belong to the Hilbert space $H^1(e_\alpha)$. The weight functions also belong to this space.

2.3. 1D discretization

The weak statement (4) can be applied to any discretization of spacetime domain with finite elements $\{e_\alpha\}$. For example, in [36], 2D discretization of (1) for the dH case (MCV) is considered and in [23,24] h-adaptive schemes are proposed, all for the cSDG method. The cSDG method can only be applied to hyperbolic PDEs, where elements are arranged in patches whose boundaries (except those on ∂D) are causal, *i.e.*, all characteristics enter or exit a *patch* of elements through the given boundary. As mentioned in §1, this work advances the earlier SDG works by solving a parabolic PDE (P in Table 1), this time in the absence of a causality constraint, and developing a quadrature-free transfer matrix solution approach for 1D. This section discusses the structured spacetime meshing and solution discretization.

2.3.1. 1D geometry

Fig. 2 shows the discretization of the spacetime domain $D\times[0,T_f]$ in Fig. 1 into triangular elements. The spatial domain is divided into N segments of size $h=L/N$, where L is the spatial size of D. The spatial position of $N+1$ base vertices $X_0=X_L$ to $X_N=X_R$ are $X_j=X_L+jh$. The temporal advance size is $\Delta t=T_f/M$, where M is the number of asynchronous time advances from time / layer 0 to time / layer $M+1$. For example, $M=4$ in the figure.

The elements are grouped in patches of one or two triangular elements. The number of elements in a patch is denoted by n_e. For example, $n_e=1$ for the patches on the left (l) and right (r) side of the domain and $n_e=2$ for the patches inside (i) the domain. Temporally, the patches are on the bottom (b), top (t), or middle (m) of the domain, colored in red, blue, or green for a few patches. Consequently, there are 9 types of patches, labeled by two letters referring to the temporal and spatial position of the patch. For example, *bi* corresponds to the (geometry of) a patch, temporally at the bottom of the domain, spatially in the interior of the domain. The treatment of the PBC requires combining the elements labeled left and right as interior patches.

2.3.2. Basis functions and element coefficients

For an element e, the primary fields T and q are discretized in spacetime as,

$$T(x,t)=\mathbb{T}(x',t')\mathbf{T}_s, \tag{5a}$$
$$q(x,t)=\mathbb{q}(x',t')\mathbf{q}_s, \tag{5b}$$

where $\mathbb{T}(x',t')$ and $\mathbb{q}(x',t')$ are spacetime basis functions, and $\mathbf{T}_s$ and $\mathbf{q}_s$ are their corresponding vectors of coefficients (unknowns). The basis functions are expressed in terms of $(x',t')=((x-x_b)/h,(t-t_b)/\Delta t)$, the local scaled Cartesian coordinate of the elements in a patch, relative to its base spacetime point (x_b,t_b). Spatially, x_b is the position of the base point (x_j) from which the patch is erected. Temporally, t_b is equal to zero and T_f for bottom and top patches, respectively, and is the center temporal position for middle patches. The position of the base point is shown by solid circle for the 9 types of patch in Fig. 2. The basis functions $\mathbb{T}$ and $\mathbb{q}$ span polynomials of order p_T and $p_q\le p_T$ in spacetime, respectively. In all the numerical examples provided in subsequent sections we use equal order polynomials $p_q=p_T$, but other choices such as $p_q=p_T-1$ can be considered. The basis vectors are expanded in terms of monomials. For example, $\mathbb{T}(x,t)=[1,x',t',x'^2,x't',t'^2]$ for $p_T=2$.

2.3.3. Element interior and boundary

Fig. 3 shows the breakdown of the elements to their interior and boundary facet types. There are two types of patches: 1) Boundary patches that are comprised of one element. For these patches $n_e=1$. Examples are patches formed by elements D and C if the vertical boundary of these elements are on Dirichlet or Neumann boundary of the domain; *cf.* (2); 2) Interior patches are comprised of two elements. The patch comprised of elements A and B is an example of all the patches with base points in the interior of the domain (X_j for $0<j<N$ in Fig. 2). Another possibility is for periodic boundary where the elements C and D play a similar role to elements A and B in the A,B patch.

We decorate any quantity associated with the interior coefficients and integrals of the patch by I. The boundary of the element is broken down to *nonvertical* and *vertical* facets, $\partial e=\partial e_{nv}\cup\partial e_v$. As shown in Fig. 3, $\partial e_{nv}=\partial e_i\cup\partial e_o$, where the inflow and outflow refers to whether the time direction enters or exits the element through the facet. There are four labels for possible vertical facets: 1, 2) The vertical facet that couples two element patches; that is ∂e_{vI} the vertical interior facet for patch A,B and ∂e_{vP} for the vertical facet of patch C,D if dealing with a problem with PBC; 3,4) ∂e_D and ∂e_N for the vertical boundary of elements C and D. In these cases, the vertical boundary of element C or D is entirely Dirichlet or Neumann.

2.3.4. Target values for 1D

For brevity, the space and time dependence of all temperature and heat flux quantities are dropped in this section. The target values for different types of the facet are provided below,

$$(T^*,q^*)=\begin{cases}(T_0,q_0) & \text{on } \partial e_i\cap\partial D_i\\ (T^-,q^-) & \text{on } \partial e_i\setminus\partial D_i\end{cases} \qquad \text{inflow boundary } \partial e_i, \tag{6a}$$
$$(T^*,q^*)=(T,q) \qquad \text{outflow boundary } \partial e_o, \tag{6b}$$

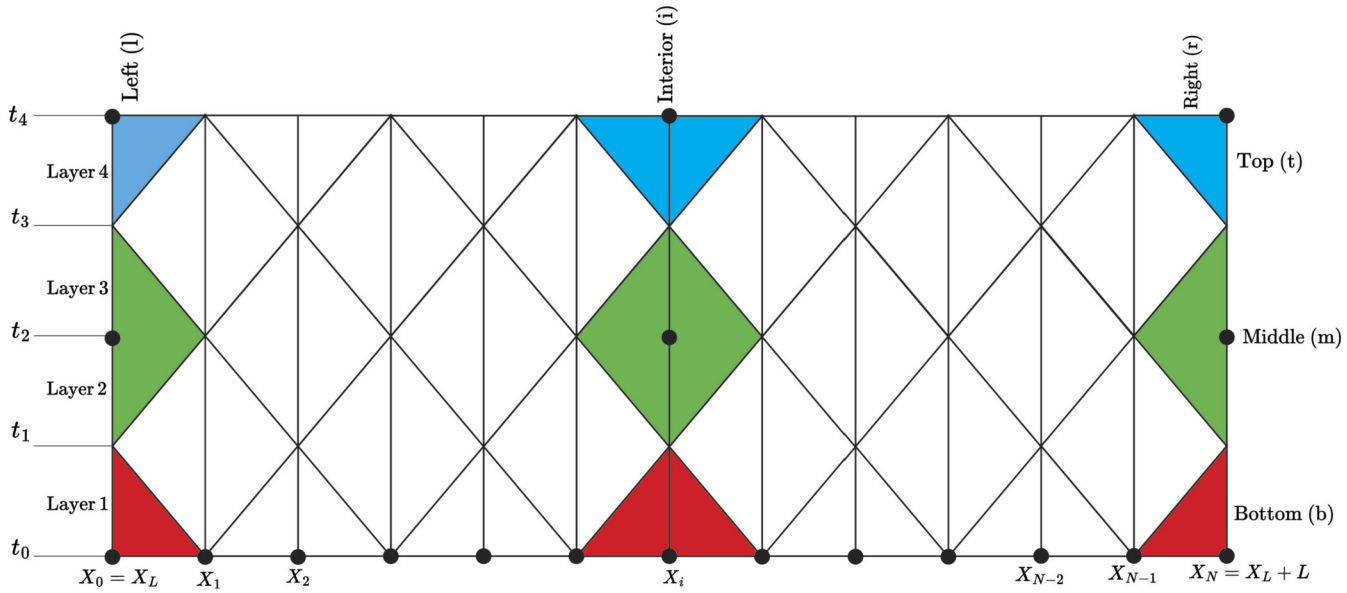

Fig. 2. The spacetime discretization of the domain shown in Fig. 1. The structured spacetime mesh includes 9 types of element erected from left ($X_0 = X_L$), right ($X_N = X_R$) and interior vertices, in bottom (red), middle (green), or top (blue) of the temporal axis. The specific labels of the elements are shown in colored elements.

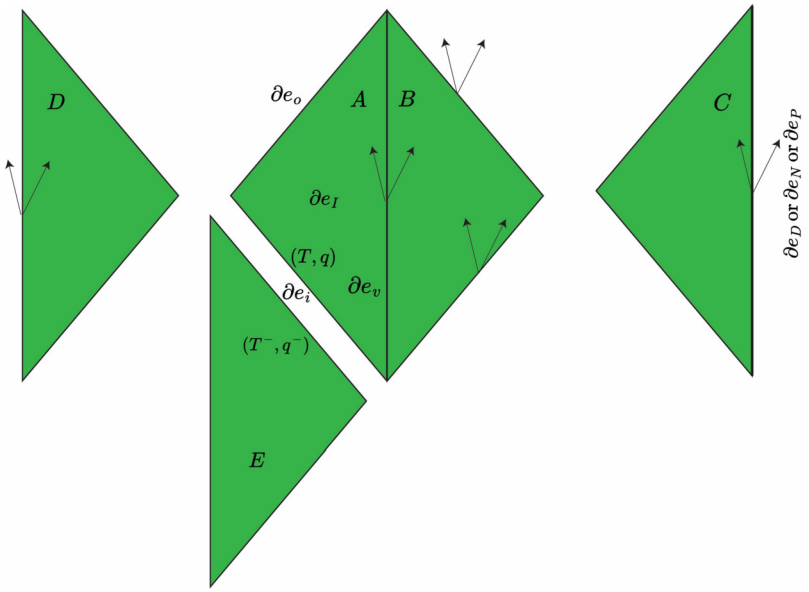

Fig. 3. Labeling of the interior or boundary of elements in spacetime for the possible forms of patches encountered. The characteristics directions (arrows) only apply to the hyperbolic PDE cases (H and dH).

$$(T^*, q_n^*) = \begin{cases} (\bar{T}, qn_x) & \text{on } \partial e_v \cap \partial D_D \\ (T, \bar{q}_n) & \text{on } \partial e_v \cap \partial D_N \\ (T^v, q^v n_x) & \text{on } \partial e_{vI} \cup \partial e_{vP} \end{cases} \quad \text{vertical boundary } \partial e_v. \quad (6c)$$

As can be seen the target values are provided for the three groups of inflow, outflow, and vertical facets. For inflow facets, if the facet is on the initial boundary of the domain, *i.e.*, $t = 0$ in Fig. 1, $n_x = 0$ and the ICs provide the target values. For the parabolic PDE case, $\tau = 0$ and q^* is not needed in the second line of (4); *cf.* (2b). When there is a predecessor neighbor element for an inflow facet, the exterior traces of temperature and heat flux are used as target fluxes in the second line of (6a). That is, for element A, the exterior traces from element E provide the target fluxes in Fig. 3. For the outflow boundaries, the interior traces provide the target values. For inflow and outflow facets $q_n^* = q^* n_x$.

For vertical facets $n_t = 0$, hence only q_n^* is needed in (4). There are three cases for target values of vertical facets. If the facet lies on the Dirichlet boundary of the domain, prescribed temperature $\bar{T}$ provides T^* whereas q_n^* is set to its interior trace qn_x. For X_0 and X_N, $n_x = -1$ and 1, respectively. In contrast, for the Neumann boundary of the domain, $q_n^* = \bar{q}_n$ and this time target temperature takes the interior trace value. Finally, for the interior vertical facet of 2-element patches, numerical fluxes (T^v, q^v) are used to obtain the target fluxes.

The numerical fluxes (T^v, q^v) depend on the traces of the fluxes from the two sides of the interface. The left and right side traces on the two sides of the interior vertical facet of a 2-element patch are denoted by (T^l, q^l) and (T^r, q^r), respectively. These correspond to elements A and B for patch A,B and C and D for patch C,D (periodic BC) in Fig. 3, respectively. For the hyperbolic PDE cases (H and dH), these target values are expressed as,

$$T^v = \frac{Z^l T^l + Z^r T^r}{Z^l + Z^r} + \frac{q^l - q^r}{Z^l + Z^r} \quad (7a)$$

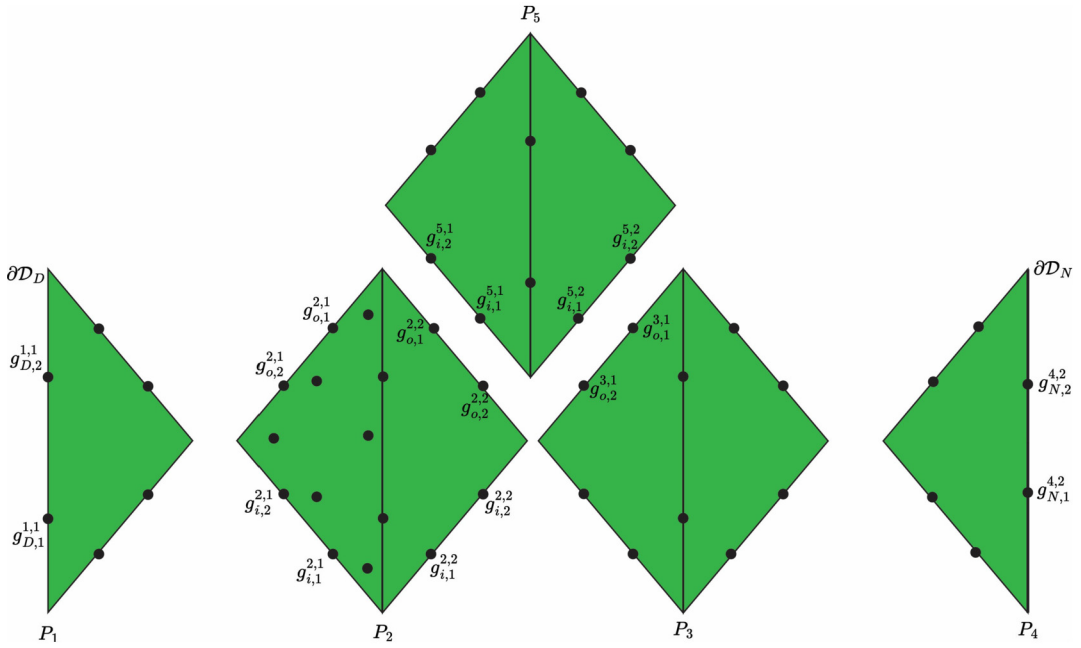

Fig. 4. The use of solutions at inflow facets, prescribed BCs, and source terms, all specified at their corresponding Gauss quadrature points, to advance the solution to the quadrature points on the outflow facets of sample patches 1 to 5.

$$q^v = \frac{Z^r q^l + Z^l q^r}{Z^l + Z^r} + \frac{Z^l Z^r}{Z^l + Z^r}\left(T^l - T^r\right) \tag{7b}$$

where $Z = cC = \sqrt{\kappa C/\tau}$ is the impedance of the material and can potentially be distinct for the two sides of the interface for bi-material interfaces. These target values are based on Riemann solutions in [41,42] and preserve the underlying characteristic structure of hyperbolic PDEs.

For the parabolic (P) PDE case, the alternating fluxes of the *Local Discontinuous Galerkin* (LDG) method [43] are used,

$$T^v = T^r, \tag{8a}$$

$$q^v = q^l. \tag{8b}$$

The alternating fluxes are used in [44,45] for parabolic PDEs. They are preferred over the central fluxes $T^v = (T^l + T^r)/2$ and $q^v = (q^l + q^r)/2$, as they provide optimal convergence rate for all polynomial orders, whereas optimal convergence rate is only achieved for even orders p_T for the central flux option.

3. Transfer matrix method

The objective of this section is to use the earlier solution at inflow facets of the patch, boundary conditions on the part of the patch that coincides with the boundary of the domain, and the source term inside the patch to update the solution on the outflow facets of a patch. Fig. 4 shows this process. Five sample patches in the domain are labeled by numbers 1 to 5. In this example, the vertical facet of patch 1 is on ∂D_D and the vertical facet of patch 4 is on ∂D_N. For these patches the solution at the quadrature points on the outflow facet depends on BCs. For all patches, the solution also depends on the solution on the inflow facets of the patch and source term inside the elements.

3.1. Quadrature points

Recall that T and q are interpolated with polynomial orders p_T and p_q. Using $p_T \geq p_q$ means that the integration order of $2p_T$ is sufficient to integrate the facet and interior terms in (4) exactly. This corresponds to numbers $n_{gf} = p_q$ and n_{gI} of Gauss quadrature points for facet and interior integration of elements, respectively. The quadrature points for $p_q = 2$ are shown by solid circles in Fig. 4, where $n_{gf} = 2$ and $n_{gI} = 6$.

The Gauss quadrature points are labeled as $g^{p,e}_{\alpha,j}$ where p is the patch number, e is the element number within a patch, α is the integration cell type, where $\alpha = i, o, v, I$ correspond to inflow, outflow, and vertical facets of the element, and I correspond to the interior of the element. Finally, j is the position of the Gauss quadrature point in its set. For $\alpha = i, o$ for each element, the numbering starts from the point closest to the vertical facet of the patch and increases outward. For vertical facet, the ordering is the from earlier to later times. The ordering of interior $\alpha = I$ quadrature points is based on the ordering of points in a Gauss quadrature point table. These quadrature orderings are shown for the all the patches in Fig. 4. The total quadrature weight for the quadrature point $g^{p,e}_{\alpha,j}$ is denoted by $w^{p,e}_{\alpha,j}$ and is equal to the Gauss quadrature weight for the parent line ($\alpha = i, o, v$) or triangle ($\alpha = I$) times the Jacobian determinant from the parent to real geometry.

3.2. Vectors of dof

We discuss the *degrees of freedom* (dof) vectors and their sizes for solution, inflow, outflow, BC, and source term groups. We start with the solution coefficient vectors $\mathbf{T}_s$ and $\mathbf{q}_s$ in (5). The number of dofs for T and q per elements are $n_T = (p_T + 1)p_T/2$ and $n_q = (p_q + 1)p_q/2$. The vector of dof (coefficients) for a patch, $\mathbf{a}_s$, and corresponding number of dofs per patch, n_s, are,

$$\mathbf{a}_s = \left[\mathbf{T}^1_s, \mathbf{q}^1_s, \cdots, \mathbf{T}^{n_e}_s, \mathbf{q}^{n_e}_s\right] \qquad n_s = n_e(n_T + n_q) \tag{9}$$

where the superscript corresponds to the element number from one to $n_e = 1$ or 2 in Fig. 4.

The inflow and outflow dof vectors are denoted by $\mathbf{a}_i$ and $\mathbf{a}_o$ and follow the quadrature point numbering discussed in §3.1, *i.e.*, starting from element one to n_e and for each element moving away from the vertical facet of the patch. The Dirichlet and Neumann BC vectors are denoted by $\mathbf{a}_D$ and $\mathbf{a}_N$ for elements with boundaries on ∂D_D and ∂D_N, respectively. They contain prescribed temperature $\bar{T}$ and $\bar{q}$ in the order of quadrature points on these facets. Finally, the source term vector $\mathbf{a}_I$ contains the source term values Q from element one to element n_e and for each in the order of interior quadrature points.

Examples of dof vectors are provided in Table 2 for patch 2 in Table 2. In this example the left and right side of the domain use Dirichlet and Neumann BCs. Correspondingly, patch 1 and 4 have nonzero

Table 2
Examples of vectors of dof for the transfer matrix method, referring to Fig. 4. The superscript for patch number is dropped for brevity.

dof type	Patch	dof vector	dof size
solution	2	$\mathbf{a}_s = [T^1_{s,1}, \cdots, T^1_{s,6}, q^1_{s,1}, \cdots, q^1_{s,6}, T^2_{s,1}, \cdots, T^2_{s,6}, q^2_{s,1}, \cdots, q^2_{s,6}]$	$n_s = n_e(n_T + n_q) = 24$
inflow	2	$\mathbf{a}_i = [\bar{T}(g^1_{i,1}), \bar{q}(g^1_{i,1}), \bar{T}(g^1_{i,2}), \bar{q}(g^1_{i,2}), \bar{T}(g^2_{i,1}), \bar{q}(g^2_{i,1}), \bar{T}(g^2_{i,2}), \bar{q}(g^2_{i,2})]$	$n_i = 2n_e n_{gf} = 8$
outflow	2	$\mathbf{a}_o = [T(g^1_{o,1}), q(g^1_{o,1}), T(g^1_{o,2}), q(g^1_{o,2}), T(g^2_{o,1}), q(g^2_{o,1}), T(g^2_{o,2}), q(g^2_{o,2})]$	$n_o = 2n_e n_{gf} = 8$
source term	2	$\mathbf{a}_I = [Q(g^1_{I,1}), \cdots, Q(g^1_{I,6}), Q(g^2_{I,1}), \cdots, Q(g^2_{I,6})]$	$n_I = n_e n_{gI} = 12$
Dirichlet BC	1	$\mathbf{a}_D = [\bar{T}(g^1_{v,1}), \bar{T}(g^1_{v,2})]$	$n_D = n_{gf} = 2$
Neumann BC	4	$\mathbf{a}_N = [\bar{q}_n(g^1_{v,1}), \bar{q}_n(g^1_{v,2})]$	$n_N = n_{gf} = 2$

Dirichlet and Neumann dof vectors in the last two rows of the table. The last column shows the general expressions of the size of dof vectors and numerical values for this example where $p_T = p_q = 2$. The last two rows only apply to 1-element patches whose vertical facets are on ∂D_D and ∂D_N. In row one, overbar refers to predecessor element or IC values for T and q, for example solutions from patches 2 and 3 for patch 4. The overbar in the last two rows corresponds to prescribed Dirichlet and Neumann BCs; *cf.* (6).

3.3. Transfer matrices

The discretization of (4) for a patch results in a linear system of equations $\mathbf{K}\mathbf{a}_s = \mathbf{F}$, where $\mathbf{K}$ is the stiffness matrix and $\mathbf{F}$ is the right hand side force vector with contributions from the source term inside the element, target values on inflow facets, and Dirichlet and Neumann boundaries of the patch. The force vector $\mathbf{F}$ can be expressed as the summation of corresponding stiffness matrices times dof vectors as shown below,

$$\mathbf{K}\mathbf{a}_s = \mathbf{F} = \mathbf{K}_I\mathbf{a}_I + \mathbf{K}_i\mathbf{a}_i + \mathbf{K}_D\mathbf{a}_D + \mathbf{K}_N\mathbf{a}_N. \tag{10}$$

The stiffness matrix $\mathbf{K}$ is of size $n_s \times n_s$. Its computation for the spacetime DG method is straightforward and can be found in [36,38,40]. The matrix $\mathbf{K}_I$ is of size $n_s \times n_I$. Its j^{th} column corresponds to the evaluation of $\hat{T}$ at the j^{th} interior quadrature point of the patch times its corresponding quadrature weight; *cf.* the fifth row of Table 2. The matrix $\mathbf{K}_i$ is of size $n_s \times n_i$. Its j^{th} column corresponds to the evaluation of the negative of the second line of (4) for the corresponding quadrature point times its quadrature weight, where $(T^* = 1, q^* = 0)$ for odd columns and $(T^* = 0, q^* = 1)$ for even columns. For example, referring to Table 2, for patch 2, the first column is the second line of (4) at $g^1_{i,1}$ for $(T^* = 1, q^* = 0)$ times $-w^1_{i,1}$, the second column is evaluated at the same point but for $(T^* = 0, q^* = 1)$ again times $-w^1_{i,1}$, all the way to column 8 (last column) for $(T^* = 0, q^* = 1)$ in the second line of (4) at $g^2_{i,2}$ times $-w^2_{i,2}$. When Dirichlet BC is present, $\mathbf{K}_D$ is an $n_s \times n_D$ matrix, whose j^{th} column is $-\hat{q}n_x$ at the quadrature point $g^1_{v,j}$ times $w^1_{v,j}$. Finally, when applicable, $\mathbf{K}_N$ is an $n_s \times n_I$ matrix, whose j^{th} column is $-\hat{T}$ at the quadrature point $g^1_{v,j}$ times $w^1_{v,j}$.

By premultiplying (10), $\mathbf{K}^{-1}$, we obtain,

$$\mathbf{a}_s = \mathcal{T}_{I\to s}\mathbf{a}_I + \mathcal{T}_{i\to s}\mathbf{a}_i + \mathcal{T}_{D\to s}\mathbf{a}_D + \mathcal{T}_{N\to s}\mathbf{a}_N, \tag{11}$$

where $\mathcal{T}_{\alpha\to s} = \mathbf{K}^{-1}\mathbf{K}_\alpha$, for $\alpha \in \{I, i, D, N\}$ are the transfer matrices from source term, inflow boundary exterior trace, Dirichlet BC, and Neumann BC to solution coefficients of the patch.

Finally, once the vector of solution dof of the patch $\mathbf{a}_s$ is obtained, the vector of dofs on the outflow facets $\mathbf{a}_o$ is obtained as,

$$\mathbf{a}_o = \mathcal{T}_{s\to o}\mathbf{a}_s \quad \Rightarrow \tag{12a}$$

$$\mathbf{a}_o = \mathcal{T}_{I\to o}\mathbf{a}_I + \mathcal{T}_{i\to o}\mathbf{a}_i + \mathcal{T}_{D\to o}\mathbf{a}_D + \mathcal{T}_{N\to o}\mathbf{a}_N, \tag{12b}$$

where $\mathcal{T}_{s\to o}$ is an $n_o \times n_s$ matrix, whose j^{th} column is T (odd j) or q (even j) at the corresponding outflow Gauss quadrature point. For example, referring to Table 2, for patch 2 in Fig. 4, first and second columns are T at q at $g^1_{o,1}$, all the way to the eighth (last) column equal to q at $g^2_{o,2}$, all as evaluation of the vector of solution dofs $\mathbf{a}_s$. Clearly, $\mathcal{T}_{\alpha\to o} = \mathcal{T}_{s\to o}\mathcal{T}_{\alpha\to s}$ for $\alpha \in \{I, i, D, N\}$ in (12b).

3.4. Implementation of transfer matrix method

The implementation is described referring to Fig. 2. The spatial points range from $X_0 = X_L$ to $X_N = X_R$. From previous section, we deal with transfer matrices for $\alpha \in \{I, i, D, N\}$ to solution dofs, $\mathcal{T}_{\alpha\to s}$ in (11), and to outflow dofs $\mathcal{T}_{\alpha\to o}$ in (12b). These along with $\mathcal{T}_{s\to o}$ in (12a) are superscripted in the general format, $\mathcal{T}^{j\tau}$ where $j \in \{0, \cdots, N\}$ is the spatial vertex index and $\tau \in \{b, m, t\}$ is the temporal shape of a patch, referring to colors red, green, and blue in the figure, respectively. For example, the transfer matrix from inflow to outflow dof vectors for $j = 1$ and middle type patch is denoted by $\mathcal{T}^{1,m}_{i\to o}$ and the inflow to solution transfer matrix for $j = 2$ and bottom type patch is denoted by $\mathcal{T}^{2,b}_{i\to s}$.

The algorithm for the solution of the spacetime is as follows:

1. Spatially discretize the domain to equal size elements, resulting in N spatial elements and $N + 1$ vertex. The extension to nonuniform spatial domain is discussed in §7.
2. Use a stable time advance Δt for all vertices. This is based on the stability analysis in §4 and the desired final time, resulting in the number of layers $M = T_f/\Delta t$.
3. For each spatial position $j \in \{0, \cdots, N\}$ compute transfer matrices $\mathcal{T}^{j\tau}_{\alpha\to s}$ and $\mathcal{T}^{j}_{s\to o}$ for $\alpha \in \{I, i, D, N\}$ that are applicable for the given j. For example, for non-periodic domain boundaries only one of $\alpha = D$ or N applies, whereas for inside and periodic boundary patches neither one applies. Moreover, if the problem has zero source term $\alpha = I$ is not needed. The calculations are for all $\tau = \{b, m, t\}$.
4. For solution layer 0 to M transfer solution to the outflow of the patches. After each advance, the outflow solution of one layer serves as the inflow for the next layer.
   For example, in Fig. 2 a typical spacetime mesh is shown for even N and $M = 4$. In solution step 0, all even numbered j vertices are pitched to $t = \Delta t$ using the bottom shape and the solution is advanced to their outflows using bottom transfer matrices. For solution layer 1, middle patches are erected on odd numbered vertices from time 0 to $2\Delta t$ and middle transfer matrices are used to transfer the solution to their outflow facet. Solution step 2 advances the solution of middle patches for even j from Δt to $3\Delta t$. Solution step 3, advances the solution of middle patches for odd j from $2\Delta t$ to $4\Delta t$. Finally, in solution step 4, the solution of top patches is used to advance the solution for even j from $3\Delta t$ to $4\Delta t$. A similar layer-by-layer process is used for other N and M.

There are a few clarifications for step 3. First, for inside j vertices that have identical materials on the two sides, the transfer matrices need to be computed only for one vertex. For example, for a problem with homogeneous material properties, only one inside the domain set of transfer matrices is needed. Second, material properties can be het-

erogeneous with constant values in spatial elements or even varying inside the elements (quadrature order can be increased). In this case, distinct transfer matrices are needed for all spatial vertices. Third, some transfer matrices are not needed, for example, $\mathcal{T}^{1,b}_{i\to s}$ in Fig. 2 for an inhomogeneous problem set-up. However, algorithmically it may be easier to compute transfer matrices for all τ for all spatial vertices that need calculation. Fourth, the indirect transfer from all α to the solution, then from the solution to outflow dof vector is only necessary if the solution coefficients are needed, for example for solution visualization. Otherwise, one can directly use inflow to outflow dof vector transfer matrices in (12b).

The transfer from the outflow of previously solved patches to the inflow of current patches in step 4 can more clearly be explained using Fig. 4. In this figure, the inflow of patch 5 is formed by the outflow of patches 2 and 3. The 8 row vector of inflow values for patch 5 is referred to as $\mathbf{a}^5_i$. It is comprised of the first 4 rows of $[\mathbf{0}_{4\times4}|\mathbb{J}_1]\mathbf{a}^2_o$ from patch 2 outflow dof vector and the second four rows of $[\mathbb{J}_1|\mathbf{0}_{4\times4}]\mathbf{a}^3_o$ from patch 3 outflow dof vector. For this example with $p_T = 2$ the matrix $\mathbb{J}_1$ is,

$$\mathbb{J}_1 = \begin{bmatrix} 0 & 0 & 1 & 0 \\ 0 & 0 & 0 & 1 \\ 1 & 0 & 0 & 0 \\ 0 & 1 & 0 & 0 \end{bmatrix}, \tag{13}$$

whereas for other p_T, $\mathbb{J}_1$ is an anti-block diagonal $2p_T \times 2p_T$ size matrix, with blocks of $[1, 0; 01]$ repeating along the upper-right to lower-left diagonal. Practically, these matrix products are avoided and the solutions from prior solutions are juxtaposed to the correct inflow dof vector positions for a new patch solution.

4. Stability analysis

4.1. Formulation of transfer matrix

For the spatially discretized form of a linear transient PDE, there exists a linear map $\mathcal{T}_{i\to o}$,

$$\mathbf{a}_o = \mathcal{T}_{i\to o}\mathbf{a}_i, \tag{14}$$

that relates the initial vector of dofs $\mathbf{a}_i$ to the final vector of dofs $\mathbf{a}_o$. The spectral stability of the solution for this map corresponds to the condition [46],

$$\rho(\mathcal{T}_{i\to o}) \le 1, \tag{15}$$

where $\rho(\mathcal{T}_{i\to o})$ is the spectral radius of $\mathcal{T}_{i\to o}$. In case of equality $\rho(\mathcal{T}_{i\to o}) = 1$, the geometric and algebraic multiplicity of the eigenvalues of $\mathcal{T}_{i\to o}$ and its normal Jordan form are needed to determine if the solution is stable or weakly, *i.e.*, linearly, unstable.

This approach is used in [47] for 1D and 2D domains with periodic boundaries to determine the stability limit of a spatial DG, temporal CK method for the parabolic heat conduction problem (P in Table 1). Uniform grids for 1D line [48] and 2D square [49] with periodic BCs are also used to study the stability (and dispersion errors) of space DG methods with Runge-Kutta and Lax-Wendroff time advancing schemes. To our knowledge, the stability analysis provided below is the first for fully discretized spacetime DG methods with temporally non-extruded girds, *e.g.* using tent-pitching meshes as the one shown in Fig. 2. This is also the very first use and stability analysis of such methods for parabolic PDEs, albeit for the 1D heat conduction problem and the type of regular grid shown in Fig. 2. As mentioned in §1, we refer to this as the tpSDG method to encompass the SDG formulations for both hyperbolic and parabolic PDEs.

Fig. 5 shows sample 1D spacetime meshes used for stability analysis of the method. The coloring convention is similar to Fig. 2. The spatial domain contains two elements of size h and PBC is used on domain boundaries. Different number of layers M from one to four are shown in the figure. Similar to Fig. 4, sample polynomial order of $p_T = 2$ is used in this figure.

Using the transfer matrices in §3.3 and time advancing procedure in §3.4, the transfer matrix in (14) is,

$$\mathcal{T}_{i\to o} = \mathcal{T}^t_{i\to o}\left(\mathbb{J}\mathcal{T}^m_{i\to o}\right)^{M-1}\mathbb{J}\mathcal{T}^b_{i\to o} \tag{16}$$

where $\mathcal{T}^b_{i\to o}$, $\mathcal{T}^m_{i\to o}$ and $\mathcal{T}^t_{i\to o}$ are the transfer matrices for bottom (red), middle (green), and top (blue) patches, as shown in the figure. The middle and top patches pitched from the periodic boundary are shown with lighter green and blue colors, respectively. The are pitched on the vertex $X_2 = X_R$ and the right side of the patch is the corresponding far left portion of the spacetime mesh on the vertex $X_0 = X_L$. These patches have identical transfer matrices to the middle and top patches pitched on X_1 with darker colors, as they have the same continuity condition and target solutions ((7) and (8) for H/dH and P PDE cases) for vertical facets. Finally, the matrix $\mathbb{J} = [\mathbf{0}, \mathbb{J}_1; \mathbb{J}_1, \mathbf{0}]$, where $\mathbb{J}_1$ is given in (13) for $p_T = 2$. This matrix maps the previous patch outflow facets to new patch inflow facets transfer and its an anti-block diagonal $4p_T \times 4p_T$ size, with blocks of $[1, 0; 01]$ repeating along the upper-right to lower-left diagonal.

4.2. Stability analysis for the hyperbolic PDE

First, we investigate the stability limit for the (undamped) hyperbolic PDE case, *i.e.*, H in Table 1. We consider a time advance in the form,

$$\Delta t = \beta\frac{h}{c}, \tag{17}$$

where h and Δt are spatial and temporal sizes for the tent pitching meshes in Fig. 5. The coefficient β is the Courant-Friedrich-Lewy (CFL) [50] time advance correction factor, where h/c is time advance dictated by the wave speed $c = \sqrt{\kappa/\tau C}$.

To obtain the stability limit for the H case, a particular value for M is chosen. Then, the correction factor β is varied and for each value of β, $\rho(\mathcal{T}_{i\to o})$ is computed. The stability limit corresponds to the value of β for which the stability condition (15) is about to be violated. This limit is denoted by β_H; that is, $\rho(\mathcal{T}_{i\to o}(\beta)) > 1$ for $\beta > \beta_H$ and $\rho(\mathcal{T}_{i\to o}(\beta)) < 1$ for $\beta < \beta_H$. The spectral radius versus β is shown in Fig. 6. First, in Fig. 6a the spacetime polynomial order of $p_T = p_q = 4$ is chosen and the stability limit is obtained for different number of layers. Clearly, independent of M, $\beta_H = 1$. Second, in Fig. 6b, motivated from the earlier result, the number of layers is fixed to $M = 10$ and the stability limit is analyzed for different polynomial orders $p_T = p_q$. Clearly, again $\beta_H = 1$ is the stability limit.

The fact that the stability (CFL) limit $\beta_H = 1$ is independent of the polynomial order (and the number of layers) is expected, as for $\beta = 1$ the spacetime inflow and outflow facets are aligned with the characteristics directions of the underlying hyperbolic PDE. These facets separate the domains of independence and influence. Under these conditions, the characteristics only enter an element through its inflow facets in Fig. 3, thus the predecessor values comprise all upstream characteristic solutions and provide the target values in (6a). Similarly, for the outflow facets, interior trace of the elements' solution provides the upstream values of all characteristics, thus resulting in interior trace target values in (6b). The stability limit $\beta_H = 1$ is sharp and geometric only. That is, independent of p_T the scheme is stable for $\beta \le 1$ and is unstable for $\beta > 1$.

In fact, the geometric stability limit of the tpSDG method for hyperbolic PDEs is one of its major advantages. For space DG methods with an explicit time marching scheme, the stability (CFL) limit β_H is severely reduced as the spatial order p_x of the method increases. For example, for *Runge-Kutta* (RK) time-marching schemes, $\beta \propto 1/p_x^2$ [49]. The situation is slightly improved for *Strong stability-preserving* (SSP) RK time integrators [51] and ADER DG method ($p_t = p_x$) [52] where the weaker scaling of $\beta \propto 1/(2p_x + 1)$ is observed [49].

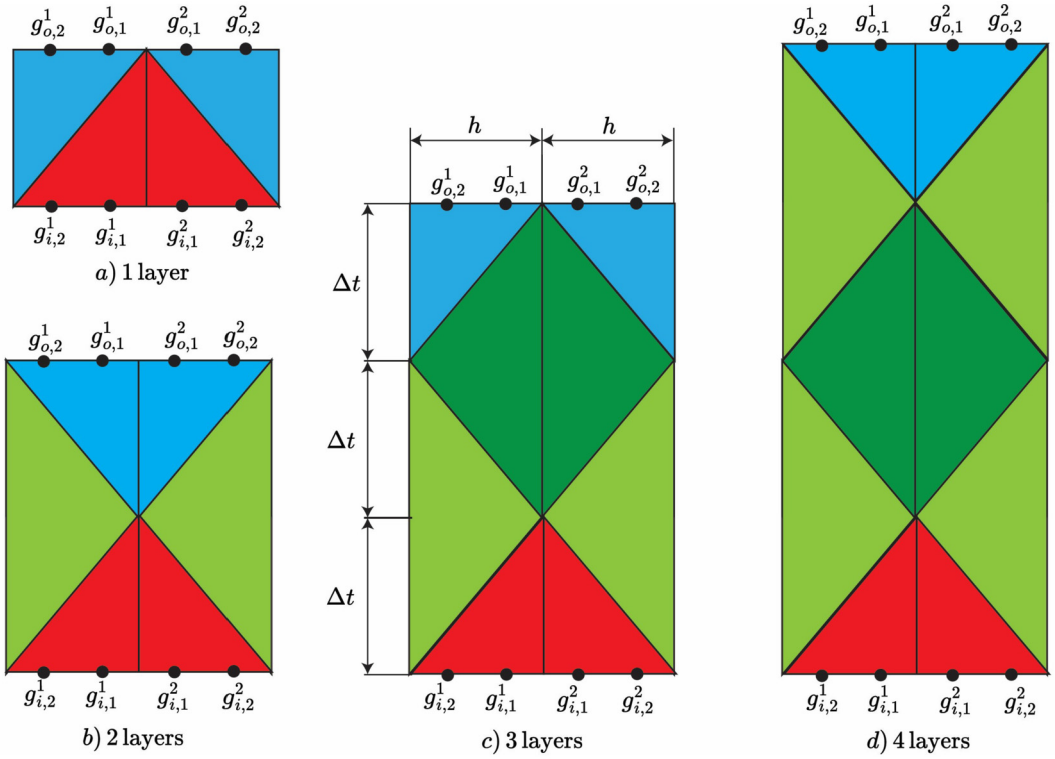

Fig. 5. Periodic domains with two spatial elements used for stability analysis of the method. The number of layers increases from one to four for a) to d). The red, green, and blue colors correspond to bottom, middle, and top patches. Lighter green and blue colors are used for patches constructed on periodic boundary $X_L = X_0$ which pairs with $X_R = X_2$.

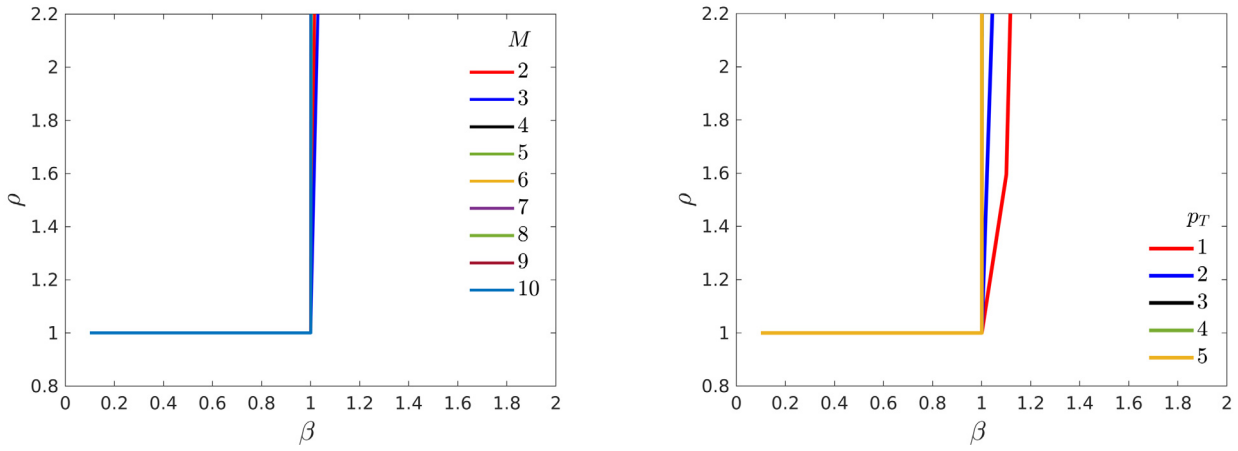

(a) The effect of number of layers M for $p_T = 4$.

(b) The effect of p_T for $M = 10$.

Fig. 6. Stability analysis for the undamped hyperbolic (H) PDE case: $\rho(\mathcal{T}_{i\to o})$ as a function of β.

The cSDG method (tpSDG method for hyperbolic PDEs) satisfies the causality condition and as shown in Fig. 6, has the optimum stability limit of $\beta_H = 1$. The energy dissipation relations of the cSDG method have been used to prove this sharp stability limit for elastodynamics [38] and electromagnetics [40]. Consequently, the cSDG method time advances are about 25 to 10 times larger than those with conventional RKDG method and SSP RK / ADER DG time integrators, respectively, for the modest space and time order of $p_T = 5$. The disparity increases as the space and time order of the method increases. Moreover, the formulation and implementation of time marching schemes with high order of accuracy have their own technical challenges, whereas the treatment of high spacetime orders in cSDG methods is trivial. These advantages for hyperbolic PDEs have been the motivation of formulation of other cSDG methods in [27–32].

4.3. Stability analysis for the parabolic PDE

Next, we investigate the stability limit for the parabolic PDE case. One main difference with the hyperbolic PDE cases is that for the parabolic case, the IC only involves initial temperature T_0 in (2a) and initial heat flux q_0 is not enforced for the parabolic case in (2b). This is consistent with having no q^* on initial front $\partial\mathcal{D}_i$ in (4) since $\tau = 0$. Thus, $n_i = 2n_{gf}$ rather than $4n_{gf}$ for the hyperbolic PDE cases as only initial temperatures are used in Fig. 5 at $t = 0$; *cf.* Table 2. Otherwise, the propagation of solution from $t = 0$ to T_f is similar to the hyperbolic cases and uses (16) to derive $\mathcal{T}_{i\to o}$. Finally, at $t = T_f$ the size of $\mathbf{a}_o$ is reduced by half by removing heat fluxes at the Gauss points. Thus, the spectral radius of $n_i \times n_i$ matrix $\mathcal{T}_{i\to o}$ for reduced $n_i = 2n_{gf}$ is used in subsequent discussion.

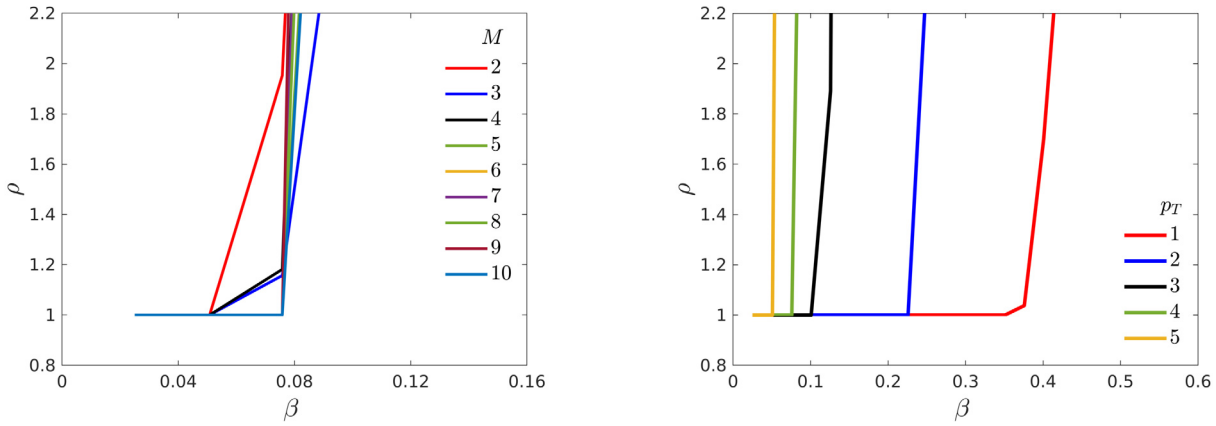

(a) The effect of number of layers M for $p_T = 4$.

(b) The effect of p_T for $M = 10$.

Fig. 7. Stability analysis for the parabolic hyperbolic (P) PDE case: $\rho(\mathcal{T}_{i\to o})$ as a function of β.

As common for explicit parabolic time marching schemes and evident from dimensional analysis, we consider a time advance in the form,

$$\Delta t = \beta \frac{h^2}{2\nu}, \tag{18}$$

where $\nu = \kappa/C$ is the diffusion coefficient and β is the time advance correction factor. The limit for which $\rho(\mathcal{T}_{i\to o}(\beta))$ exceeds from one is called the stability correction factor for the parabolic case and is denoted as β_P. Unlike the hyperbolic case, the stability limit will depend on p_T. The objective is to obtain $\beta_P(p_T)$ for different polynomial orders $p_T = p_q$.

The spectral radius versus β is shown in Fig. 7. First, in Fig. 7a the spacetime polynomial order of $p_T = p_q = 4$ is chosen and the stability limit is obtained for different number of layers. While the stability limit is tighter for $M \leq 3$, the actual unstable range of β is obtained as M increases, that is, many time advances are taken. We observe that the stability limit stabilizes for $M > 4$. Based on these observation, in Fig. 7b, 10 layers are used and p_T is varied to numerically obtain $\beta_P(p_T)$ for different polynomial orders. As expected, $\beta_P(p_T)$ decreases as p_T increases.

The stability correction factor $\beta_P(p_T)$ is provided in Table 3 for polynomial orders 1 to 5. Similar to the tpSDG method presented here, the method in [47] is arbitrary high order in space and time by using the CK solution expansion in time. Accordingly, it provides a good comparison for the stability limits in the table. The absolute values of the correction factors are very close for $p_T = 1$. Interestingly, in [47], $\beta_P(5)/\beta_P(1) \approx 0.0143$, whereas in Table 3, this decay is about 10 times larger at 0.143. That is, while the two methods start with roughly the same stability correction factors at $p_T = 1$, the tent-pitcher spacetime DG method shows a more gradual decay of β_P versus p_T. We believe the gradual tapering of elements in bottom and middle patches in Fig. 5 is favored over vertical boundaries of element in spatial DG methods (implied by explicit integration of the space solution in time) and could be a contributing factor in more gradual decay of β_P observed here. We pursue to further study this aspect in subsequent publications for nonuniform grids and 2D/3D problems.

Table 3
The stability limit correction factor $\beta_P(p_T)$ for the parabolic (P) PDE case.

	1	2	3	4	5
$\beta_P(p_T)$	0.35	0.23	0.10	0.08	0.05

5. Discussion

We discuss importance of modeling P (and dH) PDEs using the tpSDG method and the extension of the transfer matrix method to higher dimensions.

5.1. Limitation of cSDG method to hyperbolic PDEs

As discussed in §1, one main shortcoming of the cSDG method is that it can only be applied to hyperbolic PDEs. Denoting the H and P time advances from (17) and (18) as Δt_P and Δt_H, respectively, we observe $\Delta t_P/\Delta t_H \propto h/\tilde{L}$, where $\tilde{L} = \nu/c = c\tau$ is the characteristic length implied from (1). We will next discuss the effect of observation size (L) and characteristic element size h on behavior of the MCV equation.

At small L, the equation is suitable to model wave-like heat conduction. As L and corresponding h increase such that $h/\tilde{L} = \mathcal{O}(1)$ or slightly larger, Δt_P starts to be larger than Δt_H. While the cSDG method in [36] with its hyperbolic time step can still be used for all element sizes, its time advance starts to become too restrictive. As discussed in [53], for an *Asymptotic Preserving* (AP) explicit time advancing implementation of such problems, time advance should tend to the more relaxed Δt_P as the element size increases. Indeed, our stability analysis for the tpSDG method yields a loser time advance than the hyperbolic limit of the original cSDG implementation of the MCV in [36]. Finally, at much higher observation scales the MCV equation (and many other hyperbolic heat conduction models) can be very accurately represented by the parabolic heat model. Clearly, in this regime the original cSDG method cannot be applied.

The analysis proposed in the paper, albeit in 1D and for a linear PDE, is a significant advancement for the tent-pitcher spacetime DG methods and paves the way for solving more challenging and nonlinear transient PDEs such as *Navier-Stokes* (NS) equations in higher dimensions. Two key advantages of the proposed method are: 1) It can be applied to parabolic equations, *e.g.* NS and Fourier heat conduction; 2) For hyperbolic PDEs with viscous/diffusion terms and in regimes where the wave-like phenomena are still important (*e.g.* moderate sizes in the discussion of MCV), much higher time advances can be achieved by the proposed tpSDG method.

It is noted that in many instances implicit methods are favorable for problems whose explicit time advance is severely limited by parabolic operators; that is, it is affected by polynomial order and scales as h^2 (as opposed to h for hyperbolic PDEs). Examples, are the MCV equation at high observation sizes, its Fourier heat model limit, other parabolic models and idealizations, and many viscous-dominated fluid problems. However, for convection-dominated fluid problems, the proposed tpSDG method may be a viable choice by having more severe time advance limits in refined elements located in boundary layers where viscous effects are not negligible, whereas in the remainder of the domain time advances tend to those of an inviscid fluid (*i.e.*, Euler equations in [37]). These elements can be solved locally in small patches of el-

ements, as opposed to a globally coupled implicit solver, and can be arbitrarily high order in spacetime.

5.2. Extensibility of the transfer matrix method to higher dimensions

The extension of the transfer matrix approach to 2D and 3D problems can be challenging. One approach is the derivation of these matrices for uniform grids. The advantage is that all the relevant matrices can be precomputed and tabulated similar to FD update equations. A similar approach is proposed in [54], where certain transformations of a Trefftz method on a uniform 2D rectangular grid are precomputed. Therein, 5 shapes of spacetime elements are encountered inside the domain. A 2D/3D version of the proposed transfer matrix requires precomputing certain number of patch geometries with vertices inside the domain, on surfaces (3D), on boundary lines, and corners, which can be a challenging task.

The second approach is more practical by precomputing transfer matrices for any given mesh at the beginning of the simulation. Not only unstructured spatial meshes can be used in 2D and 3D with heterogeneous material fields, the precomputation of transfer matrices is algorithmically much simpler in this approach; for each vertex in the spatial domain only bottom, middle, and top (if flat final fronts are desired) patches with a chosen layer time advance of Δt need to be precomputed. All further patch solutions simply uses these precomputed transfer matrices. This approach is deemed to be faster than Trefftz methods as it requires minimal calculations at the quadrature points and no matrix solution is required. In addition, similar to all other spacetime DG methods it can be arbitrarily high order (by choosing a given p in precomputation stage).

The drawbacks of the transfer matrix approach are its applicability to linear PDEs in the present form and using a global layer time advance Δt, that is determined by stability limit of all spatial elements. Still, all the linear PDEs discussed in DG Trefftz method [27–32] can also benefit from fast calculations of extensions of this transfer matrix method in 2D and 3D.

6. Numerical examples

We first examine the accuracy of the transfer matrix approach by solving problems with exact solution. For this purpose, the orders of accuracy of all PDE types are numerically investigated in §6.1. This is followed by a 1D heat conduction problem in §6.2 for the three PDE types. The second set of examples in §6.3 apply the method to an inhomogeneous domain. Time advances for H and dH cases satisfy the causality condition $\beta \leq 1$ in (17), and for parabolic PDEs $\beta < \beta_P(p_T)$ (see Table 3) is used. For the examples in §6.3, the stability correction factor is taken as the smallest value across all spatial elements in the domain.

6.1. Convergence rate study

For the convergence studies, we consider harmonic exact solutions $T(x,t) = \Re(\exp(i(kx - \omega t)))$, where $\Re$ is the real part operator, $i = \sqrt{-1}$, k is the wavenumber, and ω is the frequency. We choose $k = 2\pi$, corresponding to a full spatial wave in the domain $[0,1]$. Dirichlet BCs at $x = 0$ and 1, and IC for T are applied based on $T(x,t)$. All nonzero material properties in Table 1 are equal to one. The complex-valued $\omega(k)$ is obtained by plugging harmonic temperature (and heat flux) in (1). For example, for H and P types, we have $w(k) = ck$ and $-ivk^2$, respectively. The final time is $T_f = 1$ for all PDEs and the L2 errors between exact (T and q) and discrete (T^h and q^h) solutions are computed over the entire spacetime volume. Spatial mesh resolutions of $h = 1/2$ to $h = 1/128$ with powers of 2 and polynomial orders of $p_T = 0$ to $p_T = 5$ are used for this study. The base of logarithms in the plots is 10. The same order is used for heat flux; that is $p_q = p_T$. Riemann fluxes (7) are used for H and dH PDEs and alternating fluxes (8) are used for the P PDE. The CFL number of $\beta = 1$ is used for H and dH PDEs and the time advance of P PDE is determined based on correction factors in Table 3.

Table 4
The number of layers for the examples in §6.2 for all PDE types.

PDE\n_e	2	4	8	16	32	64	128
H, dH	6	12	15	30	60	100	195
P, $p_T = 1$	48	150	600	Not used			
P, $p_T = 3$	120	480	1920				

Fig. 8 shows the convergence rates for all PDE types. As can be observed, the convergence rate for T is $p_T + 1$ for all cases, which is the optimal convergence rate. We note that in terms of energy dissipation error, we had obtained optimal convergence rates for hyperbolic elastodynamic [38] and electromagnetic [40] PDEs. There is, however, a nuanced behavior for the P PDE; as shown in (8d) the odd polynomial orders have the suboptimal convergence order of p_T for q. While the detailed mathematical analysis of such suboptimal convergence rate in this context is lacking, we refer to discussions in [44] in that certain flux options for parabolic PDEs can result in such subptimal orders for odd orders p_T ($= p_q$) in space DG methods. For H and dH types, the convergence rates for q is optimal at $p_T + 1$ for all polynomial orders (not shown for brevity).

6.2. Heat conduction from left to right of a 1D domain

The heat conduction from the left to the right side of the domain is considered. Dirichlet BC is used on both sides with $\bar{T} = 1$ and 0 on the left and right side of the domain, respectively. ICs are $T_0 = 0$ and $q_0 = 0$ in $\mathcal{D}$. dH, H, and P cases are considered in order, although the H case is a wave equation, it is included for comparison with the MCV and Fourier heat models. The material properties are $\tau = 1$ (for hyperbolic cases), $\kappa = 1$, and $C = 1$. Before discussing the results, we present the number of layers used for each PDE type and mesh resolution in Table 4 to demonstrate much master growth of the number of layers for the parabolic case. As mentioned earlier, for H and dH cases, the CFL number of one is used whereas for the parabolic case the correction factors from Table 3 are used to determine Δt from (18). In all cases, the time step is decreased to have tent pole tops at sampling times of 0.5 and 1.5 to more easily extract the discrete solution at these times.

6.2.1. Damped hyperbolic solution

Fig. 9 shows the solutions of the damped hyperbolic equation for $p_T = 1$ and 3 at times $t = 0.5$ and 1.5 for $n_e = 2$ to 256. The spatial domain is $\mathcal{D} = [0,1]$. The exact solution is provided in [55]. As evident, there is a sharp wave front at $x = 0.5$ for $t = 0.5$ as the wave speed is 1. The reflected front wave is again at $x = 0.5$ for $t = 1.5$. As expected, numerical solutions tend to the exact solution as the mesh resolution increases, and $p_T = 3$ solutions are superior to those for $p_T = 1$, especially for low mesh resolutions.

The effect of polynomial order on solution is studied in Fig. 10 for a domain with $n_e = 32$ and $p_T = 0$ to 4. The solution does not exhibit over and undershoot for $p_T = 0$, but is overly damped. The solution tends to the exact solution as p_T is enriched with local over and undershoot for all $p_T > 0$. Finally, Fig. 11 depicts the solution in spacetime for $n_e = 32$ and $p_T = 3$. The clear wave front along $x = t$ line and its reflection from the right interface can clearly be seen in the figure. The decay of the temperature along the x axis is attributed to the damped nature of the MCV equation.

We note that for almost all solutions in Fig. 9 and Fig. 10, there are overshoots and undershoots around the discontinuity that do not tend to zero as the mesh resolution increases. We refer the reader to [37] for more detailed discussion of tendency of $p > 0$ solutions to overshoot and undershoot around solution discontinuities. For nonlinear PDEs, limiters [37], and artificial diffusion [56] are used in the SDG method to

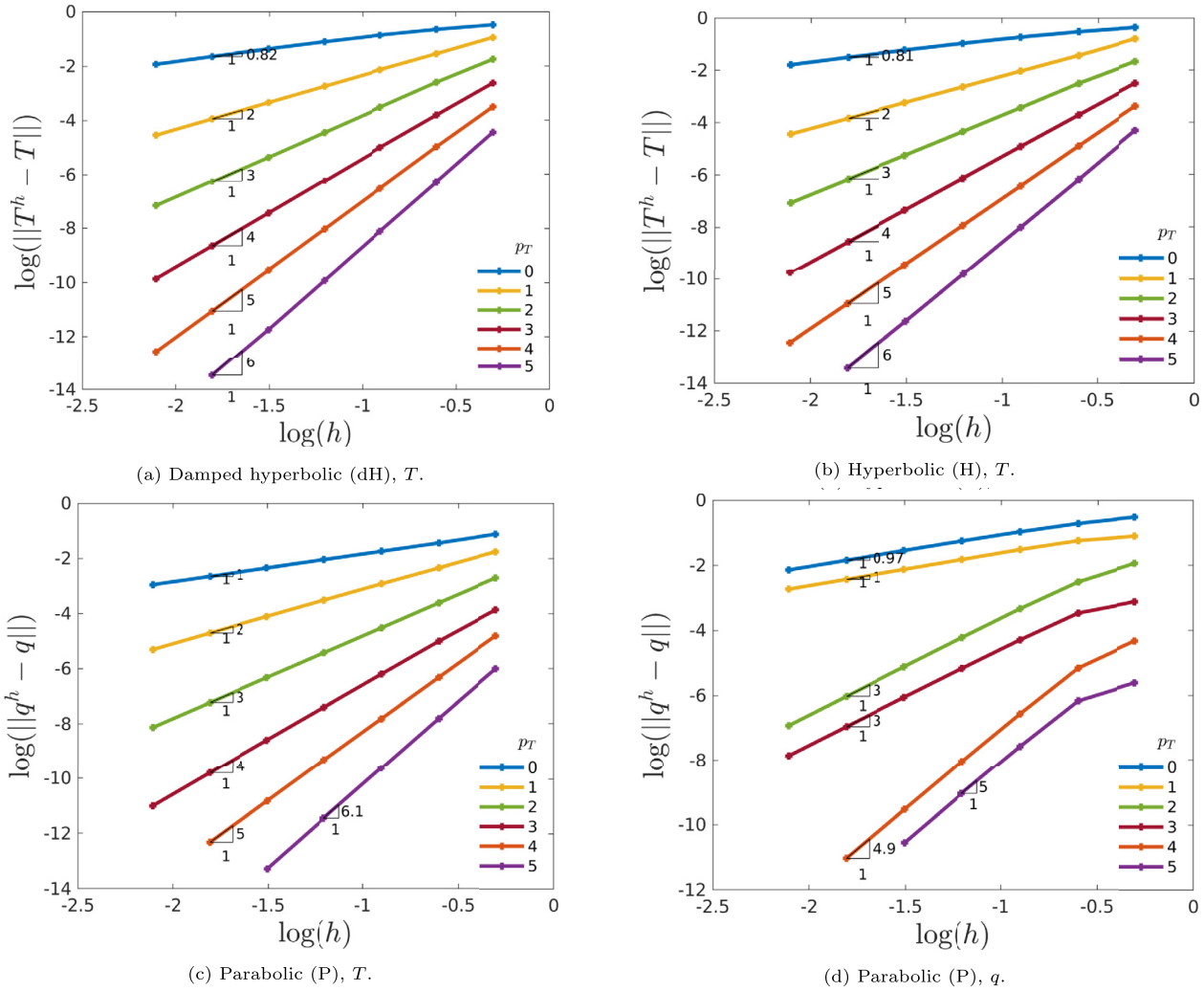

(a) Damped hyperbolic (dH), T.

(b) Hyperbolic (H), T.

(c) Parabolic (P), T.

(d) Parabolic (P), q.

Fig. 8. Convergence rates of the L2 error norm of the numerical solution versus the exact solution for the three PDE types.

improve the accuracy of the solution around shocks and contact discontinuities and, when applicable, prevent such over/undershoots render the solutions unstable. However, for the linear PDEs considered herein, these overshoots and undershoots are benign. As an alternative, $p = 0$ solutions generally eliminates these features, although with the tendency of significantly diffusing the wave fronts; *cf.* Fig. 10.

6.2.2. Undamped hyperbolic solution

The undamped hyperbolic PDE corresponds to the wave equation in Table 1. Fig. 12 shows the solutions at $t = 0.5$ and 1.5 for $p_T = 1$ and 3. The spatial domain is $D = [0, 1]$. The exact solution is an undamped wave moving to the right with speed $c = 1$ with front and reflected front at $x = 0.5$ for $t = 0.5$ and 1.5, respectively. The accuracy of numerical solutions are qualitatively similar to the damped hyperbolic case.

The effect of polynomial order is studied in Fig. 13, where again the solution for $p_T = 0$ is overdamped but without over and undershoot. The spacetime solution for T is shown in Fig. 14 for $n_e = 32$ and $p_T = 3$. The undamped wave of magnitude one and speed one is reflected at time one from the right boundary. The numerical solution is clean as there is little disturbance around the moving sharp wave front.

6.2.3. Parabolic equation

For the parabolic solution, the larger domain of $D = [0, 3]$ is chosen to better demonstrate the exponential decay of solution in space. Exact solution of this problem is $\mathrm{erfc}(x/2\sqrt{\frac{t}{C}})$, where erfc is the complementary error function. Fig. 15 shows the solutions for $p_T = 1$ and 3 for $t = 0.5$. The numerical solutions are closer to the exact solution compared to hyperbolic PDE cases as for the parabolic case there is no sharp moving wave front. This is specially true for $p_T = 3$, as unlike the hyperbolic cases the exact solution is sufficiently smooth. Moreover, the solution is mathematically nonzero across the entire domain immediately after $t > 0$. Numerically, the nonzero solution moves one element to the right as time advances one layer at a time. But the time advance in the form (18) and $\beta < \beta_P$ ensures the convergence to the exact solution and accurate tracking of the *approximate wave front*, for example when the argument of erfc is around 2.

6.3. MCV equation with inhomogeneous κ

This example demonstrates that the transfer matrix approach can be applied to problems with inhomogeneous material properties. As described in §3.4, for each vertex inside the domain, bottom, middle, and top transfer matrices need to be precomputed. For homogeneous domains, only one such precomputation is needed for all vertices inside the domain.

Material properties are as follows: $\tau = 1$, $C = 1$, and for conductivity two cases of $\kappa(x) = 10x + 1$ and $\kappa(x) = (10x + 1)^2$ are considered. These cases correspond to wave speeds of $c = \sqrt{10x + 1}$ and $c = 10x + 1$, respectively, with the latter representing a more heterogeneous example. The ICs are $T_0 = 1$ and $q_0 = 0$ in $D = [0, 1]$, and the final time is $T_f = 1$. The spatial element size is $h = 0.02$. The Dirichlet BCs are $\bar{T} = 2$ and 0 for the left and right sides of the domain, respectively.

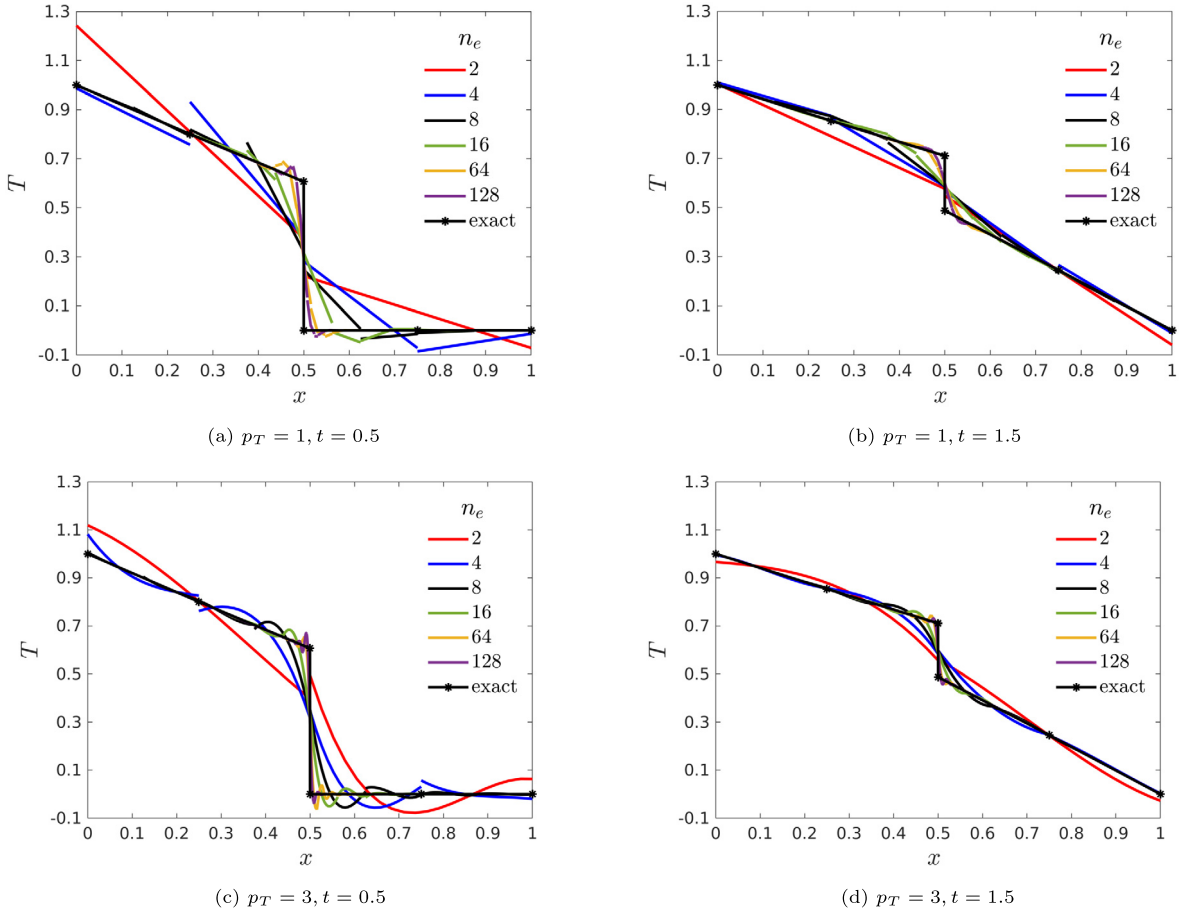

(a) $p_T = 1, t = 0.5$ (b) $p_T = 1, t = 1.5$

(c) $p_T = 3, t = 0.5$ (d) $p_T = 3, t = 1.5$

Fig. 9. Solutions for the damped hyperbolic equation for polynomial orders $p_T = 1$ and 3 at times $t = 0.5$ and 1.5.

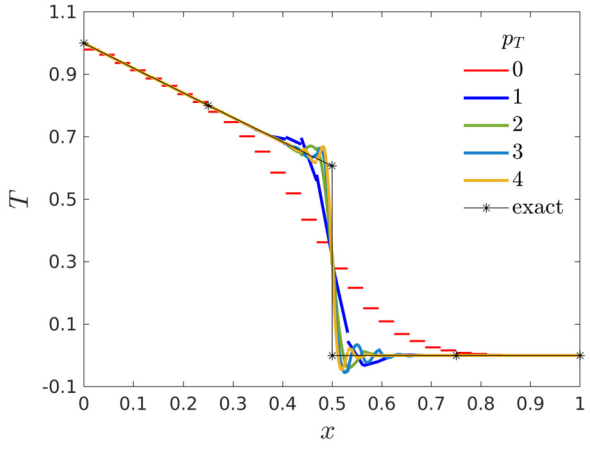

Fig. 10. Comparison of solutions for $n_e = 32$ and different p_T for the damped hyperbolic equation at $t = 0.5$.

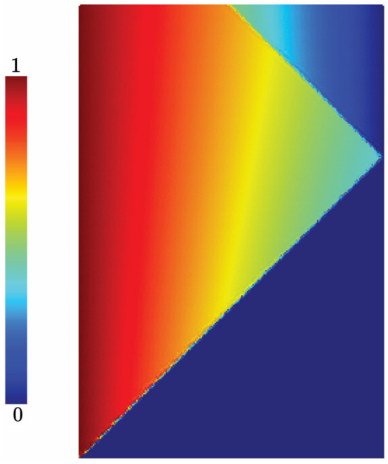

Fig. 11. Damped hyperbolic solution for T in spacetime domain $[0, 1] \times [0, 1.5]$ (time along the vertical axis) for $p_T = 3$ and $n_e = 32$.

Fig. 16 shows the spacetime temperature solutions for the two κ cases. In both cases there is a region with $T = 1$ above the initial condition and two waves with starting temperatures of 2 and 0 enter the domain from the left and right sides, respectively. These two waves collide at time around 0.28 in Fig. 16a and at an earlier time around 0.15 in Fig. 16b. From the wave fronts it is evident that the wave speed is higher on the right side, thus the intersection positions are closer to the left side of the domain. This effect is more pronounced for $\kappa(x) = (10x + 1)^2$ due to its higher and more heterogeneous wave speeds. For $\kappa(x) = 10x + 1$, the right-going wave accelerates after this intersection. This and the left-going wave reflect from the right and left boundaries at time around 0.55.

7. Conclusions

We presented a spacetime DG method where vertices from a 1D uniform space mesh are pitched in time to advance the solution. Unlike the cSDG method, this so-called tpSDG method can be applied to both hyperbolic and parabolic PDEs. The transfer matrix approach provides a quadrature-free solution process, where during the initialization

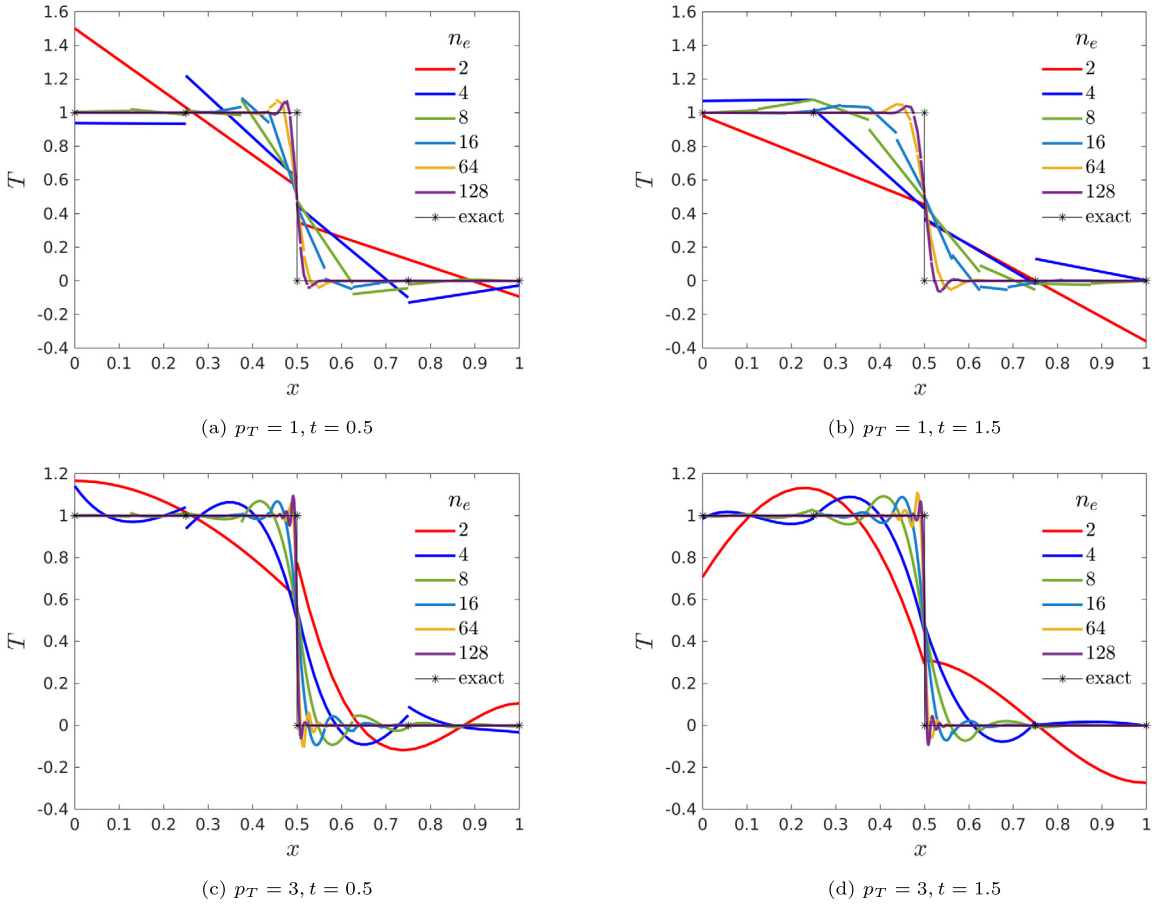

(a) $p_T = 1, t = 0.5$ (b) $p_T = 1, t = 1.5$

(c) $p_T = 3, t = 0.5$ (d) $p_T = 3, t = 1.5$

Fig. 12. Solutions for the undamped hyperbolic equation for polynomial orders $p_T = 1$ and 3 at times $t = 0.5$ and 1.5.

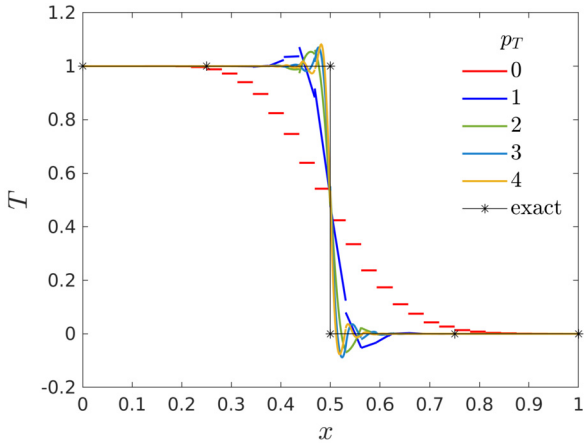

Fig. 13. Comparison of solutions for $n_e = 32$ and different p_T for the undamped hyperbolic equation at $t = 0.5$.

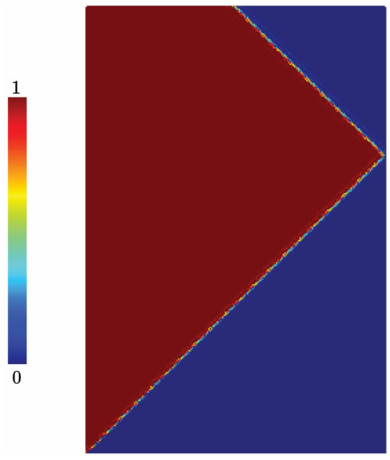

Fig. 14. Undamped hyperbolic solution for T in spacetime domain $[0, 1]\times[0, 1.5]$ (time along the vertical axis) for $p_T = 3$ and $n_e = 20$.

stage transfer matrices that map inflow, boundary, and source terms to solution coefficients are computed. Using the solution coefficient to outflow map, the previous values are then mapped to the outflow of the elements, or the intermediate step is avoided if the explicit form of spacetime solution is not sought. The resulting scheme resembles a finite difference method with the difference that the stencil points are at the Gauss points of inflow, outflow, and domain boundary facets of spacetime elements, hence proving a systematic way to simultaneously increase the order in space and time. The spectral stability analysis of the method provides the sharp CFL limit of one for the hyperbolic PDE case, confirming the polynomial independent stability limit of cSDG methods [36,38–40]. The extension of the tpSDG method to parabolic methods is new with time advances proportional to the square of element size times now a polynomial-dependent correction factor.

Two extensions of this work are discussed next. First, the tpSDG method can be extended to other parabolic PDEs such as the Navier-Stokes equation. Similar to [47] this method will be asynchronous with arbitrarily tunable spacetime order of accuracy; based on the 1D stability results presented herein, we expect it to still have looser stability correction factors than [47]. Moreover, treatment of nonlinearities will be much more straightforward than CK-DG and ADER-DG methods.

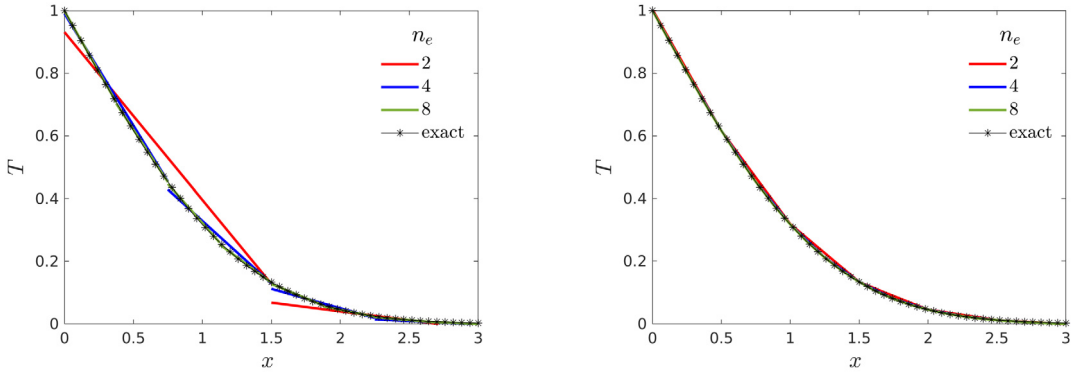

(a) $p_T = 1$. (b) $p_T = 3$.

Fig. 15. Solutions for the parabolic equation for polynomial orders $p_T = 1$ and 3 at time $t = 0.5$.

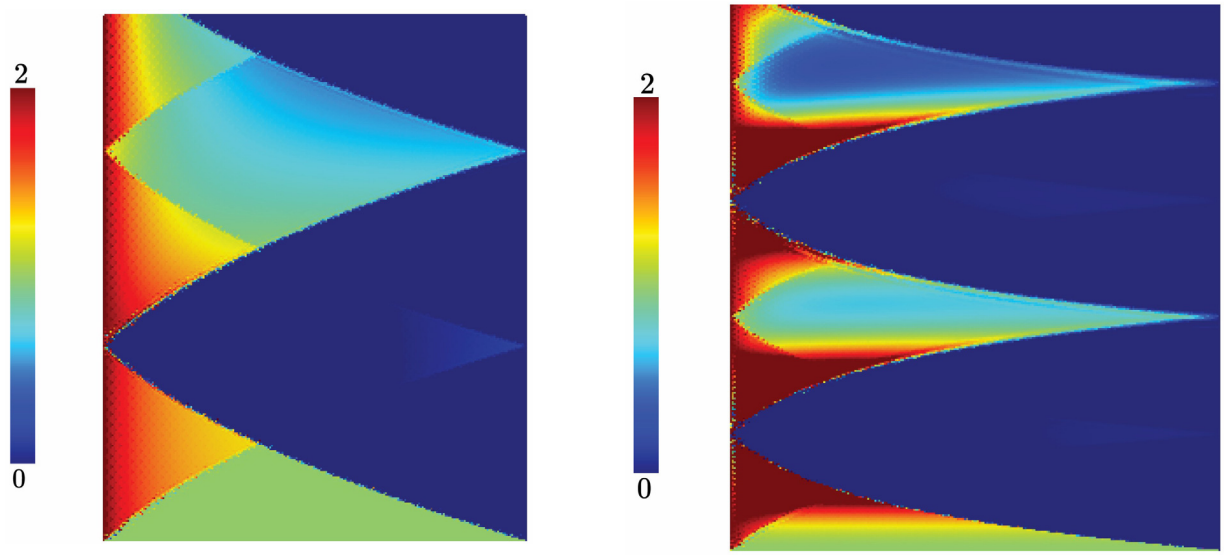

(a) $\kappa(x) = 10x + 1$. (b) $\kappa(x) = (10x + 1)^2$.

Fig. 16. The spacetime temperature solutions for the MCV problem with inhomogeneous κ. Time is along the vertical axis.

Second, if a temporarily uniform time advance is used for all spatial vertices, the transfer matrix approach can be extended to higher dimensions and nonuniform simplicial discretization of the spatial domain for linear transient PDEs. Similar to the 1D case, material heterogeneity can be modeled. During the initialization stage transfer matrices for bottom, middle, and top patches are precomputed for each spatial vertex. The advantage of such method will be a very fast solution update for linear transient PDEs with arbitrarily tunable order of accuracy in spacetime.

Data availability

The data that has been used is confidential.

Acknowledgement

The authors acknowledge partial support for this work via the U.S. National Science Foundation (NSF) CCF - Scalable Parallelism in the Extreme (SPX) program grant number 1725555 and (NSF) CMMI - Mechanics of Materials and Structures (MoMS) program grant number 2039472 to the University of Tennessee Space Institute.

References

[1] Jan S. Hesthaven, Tim Warburton, Nodal Discontinuous Galerkin Methods: Algorithms, Analysis, and Applications, Springer Science & Business Media, 2007.

[2] Béatrice Rivière, Discontinuous Galerkin Methods for Solving Elliptic and Parabolic Equations: Theory and Implementation, SIAM, 2008.

[3] Bernardo Cockburn, Chi-Wang Shu, Runge–Kutta discontinuous Galerkin methods for convection-dominated problems, J. Sci. Comput. 16 (3) (2001) 173–261.

[4] Bernardo Cockburn, George E. Karniadakis, Chi-Wang Shu, Discontinuous Galerkin Methods: Theory, Computation and Applications, vol. 11, Springer Science & Business Media, 2012.

[5] Chi-Wang Shu, Discontinuous Galerkin method for time-dependent problems: survey and recent developments, in: Recent Developments in Discontinuous Galerkin Finite Element Methods for Partial Differential Equations, 2014, pp. 25–62.

[6] Janivita Joto Sudirham, Jacobus J.W. van der Vegt, Rudolf M.J. van Damme, Space–time discontinuous Galerkin method for advection–diffusion problems on time-dependent domains, Appl. Numer. Math. 56 (12) (2006) 1491–1518.

[7] Christiaan M. Klaij, Jaap J.W. van der Vegt, Harmen van der Ven, Space–time discontinuous Galerkin method for the compressible Navier–Stokes equations, J. Comput. Phys. 217 (2) (2006) 589–611.

[8] Sander Rhebergen, Bernardo Cockburn, Jaap J.W. Van Der Vegt, A space–time discontinuous Galerkin method for the incompressible Navier–Stokes equations, J. Comput. Phys. 233 (2013) 339–358.

[9] Miloslav Feistauer, Jaroslav Hajek, Karel vadlenka, Space-time discontinuos Galerkin method for solving nonstationary convection-diffusion-reaction problems, Appl. Math. 52 (3) (2007) 197–233.

[10] Miloslav Feistauer, Vaclav Kucera, Karel Najzar, Jaroslava Prokopova, Analysis of space-time discontinuous Galerkin method for nonlinear convection-diffusion problems, Numer. Math. 117 (2) (2011) 251–288.

[11] Jan Cesenek, Miloslav Feistauer, Theory of the space-time discontinuous Galerkin method for nonstationary parabolic problems with nonlinear convection and diffusion, SIAM J. Numer. Anal. 50 (3) (2012) 1181–1206.

[12] Bo Wang, Ziqing Xie, Zhimin Zhang, Space-time discontinuous Galerkin method for Maxwell equations in dispersive media, Acta Math. Sci. 34 (5) (2014) 1357–1376.
[13] Tamás L. Horváth, Sander Rhebergen, An exactly mass conserving space-time embedded-hybridized discontinuous Galerkin method for the Navier–Stokes equations on moving domains, J. Comput. Phys. 417 (2020) 109577.
[14] M. Lilienthal, S.M. Schnepp, T. Weiland, Non-dissipative space-time *hp*-discontinuous Galerkin method for the time-dependent Maxwell equations, J. Comput. Phys. 275 (2014) 589–607.
[15] Jonas D. De Basabe, Mrinal K. Sen, Stability of the high-order finite elements for acoustic or elastic wave propagation with high-order time stepping, Geophys. J. Int. 181 (1) (2010) 577–590.
[16] T. Schwartzkopff, C.D. Munz, E.F. Toro. ADER, A high-order approach for linear hyperbolic systems in 2D, J. Sci. Comput. (17) (2002) 231–240.
[17] T. Schwartzkopff, M. Dumbser, C.-D. Munz, Fast high order ADER schemes for linear hyperbolic equations, J. Comput. Phys. 197 (2) (2004) 532–539.
[18] M. Dumbser, C.-D. Munz, ADER discontinuous Galerkin schemes for aeroacoustics, C. R. Acad. Sci., Sér. IIb, Méc. 333 (9) (2005) 683–687.
[19] M. Dumbser, C.-D. Munz, Building blocks for arbitrary high order discontinuous Galerkin schemes, J. Sci. Comput. 27 (1–3) (2006) 215–230.
[20] G.R. Richter, An explicit finite element method for the wave equation, Appl. Numer. Math. 16 (1–2) (1994) 65–80.
[21] Richard S. Falk, Gerard R. Richter, Explicit finite element methods for symmetric hyperbolic equations, SIAM J. Numer. Anal. 36 (3) (1999) 935–952.
[22] Jeff Erickson, Damrong Guoy, A. Üngör, J. Sullivan, Building spacetime meshes over arbitrary spatial domains, in: Proceedings of the 11th International Meshing Roundtable, 2002, pp. 391–402.
[23] Reza Abedi, Shuo-Heng Chung, Jeff Erickson, Yong Fan, Michael Garland, Damrong Guoy, Robert Haber, John M. Sullivan, Shripad Thite, Yuan Zhou, Spacetime meshing with adaptive refinement and coarsening, in: Proceedings of the Twentieth Annual Symposium on Computational Geometry, SCG '04, Brooklyn, New York, USA, June 9-11 2004, ACM, 2004, pp. 300–309.
[24] Reza Abedi, Robert B. Haber, Shripad Thite, Jeff Erickson, An *h*–adaptive spacetime–discontinuous Galerkin method for linearized elastodynamics, Eur. J. Comput. Mech. 15 (6) (2006) 619–642.
[25] Reza Abedi, Shuo-Heng Chung, Morgan A. Hawker, Jayandran Palaniappan, Robert B. Haber, Modeling evolving discontinuities with spacetime discontinuous Galerkin methods, in: IUTAM Symposium on Discretization Methods for Evolving Discontinuities, IUTAM, in: IUTAM Bookseries, vol. 5, Springer, 2007, pp. 59–87.
[26] Reza Abedi, Robert B. Haber, Philip L. Clarke, Effect of random defects on dynamic fracture in quasi-brittle materials, Int. J. Fract. 208 (1–2) (2017) 241–268.
[27] Jay Gopalakrishnan, Peter Monk, Paulina Sepúlveda, A tent pitching scheme motivated by Friedrichs theory, Comput. Math. Appl. 70 (5) (2015) 1114–1135.
[28] Hélène Barucq, Henri Calandra, Julien Diaz, Elvira Shishenina, Space-time Trefftz-discontinuous Galerkin approximation for elasto-acoustics, PhD thesis, Inria Bordeaux Sud-Ouest, 2017, UPPA (LMA-Pau);Total E&P.
[29] Andrea Moiola, Ilaria Perugia, A space–time Trefftz discontinuous Galerkin method for the acoustic wave equation in first-order formulation, Numer. Math. 138 (2) (2018) 389–435.
[30] Hélène Barucq, Henri Calandra, Julien Diaz, Elvira Shishenina, Space–time Trefftz-DG approximation for elasto-acoustics, Appl. Anal. 99 (5) (2020) 747–760.
[31] Ilaria Perugia, Joachim Schöberl, Paul Stocker, Christoph Wintersteiger, Tent pitching and Trefftz-DG method for the acoustic wave equation, Comput. Math. Appl. 79 (10) (2020) 2987–3000.
[32] Dow Drake, Jay Gopalakrishnan, Joachim Schöberl, Christoph Wintersteiger, Convergence analysis of some tent-based schemes for linear hyperbolic systems, Math. Comput. 91 (334) (2022) 699–733.
[33] Claes Johnson, Uno Nävert, Juhani Pitkäranta, Finite element methods for linear hyperbolic problems, Comput. Methods Appl. Mech. Eng. 45 (1–3) (1984) 285–312.
[34] Carlo Cattaneo, Sur une forme de l'equation de la chaleur eliminant la paradoxe d'une propagation instantantee, C. R. Acad. Sci. 247 (1958) 431–433.
[35] Pierre Vernotte, Les paradoxes de la theorie continue de l'equation de la chaleur, C. R. Acad. Sci. 246 (1958) 3154.
[36] Scott T. Miller, Robert B. Haber, A spacetime discontinuous Galerkin method for hyperbolic heat conduction, Comput. Methods Appl. Mech. Eng. 198 (2) (2008) 194–209.
[37] J. Palaniappan, Robert B. Haber, R.L. Jerrard, A spacetime discontinuous Galerkin method for scalar conservation laws, Comput. Methods Appl. Mech. Eng. 193 (2004) 3607–3631.
[38] Reza Abedi, Robert B. Haber, Boris Petracovici, A spacetime discontinuous Galerkin method for elastodynamics with element-level balance of linear momentum, Comput. Methods Appl. Mech. Eng. 195 (2006) 3247–3273.
[39] Raj Kumar Pal, Reza Abedi, Amit Madhukar, Robert B. Haber, Adaptive spacetime discontinuous Galerkin method for hyperbolic advection-diffusion with a nonnegativity constraint, Int. J. Numer. Methods Eng. 105 (13) (2016) 963–989.
[40] R. Abedi, S. Mudaliar, An asynchronous spacetime discontinuous Galerkin finite element method for time domain electromagnetics, J. Comput. Phys. 351 (Supplement C) (2017) 121–144.
[41] Reza Abedi, Robert B. Haber, Riemann solutions and spacetime discontinuous Galerkin method for linear elastodynamic contact, Comput. Methods Appl. Mech. Eng. 270 (2014) 150–177.
[42] Reza Abedi, Robert B. Haber, Spacetime simulation of dynamic fracture with crack closure and frictional sliding, Adv. Model. Simul. Eng. Sci. 5 (1) (2018) 22, Equal contribution authorship.
[43] Bernardo Cockburn, Chi-Wang Shu, The local discontinuous Galerkin method for time-dependent convection-diffusion systems, SIAM J. Numer. Anal. 35 (6) (1998) 2440–2463.
[44] C.W. Shu, Different formulations of the discontinuous Galerkin method for the viscous terms, in: Z.-C. Shi, M. Mu, W. Xue, J. Zou (Eds.), Advances in Scientific Computing, 2001.
[45] Robert M. Kirby, George Em Karniadakis, Selecting the numerical flux in discontinuous Galerkin methods for diffusion problems, J. Sci. Comput. 22 (1) (2005) 385–411.
[46] Charles Hirsch, Numerical Computation of Internal & External Flows: Fundamentals of Numerical Discretization, John Wiley & Sons, Inc., 1988.
[47] Frieder Lörcher, Gregor Gassner, Claus-Dieter Munz, An explicit discontinuous Galerkin scheme with local time-stepping for general unsteady diffusion equations, J. Comput. Phys. 227 (11) (2008) 5649–5670.
[48] He Yang, Fengyan Li, Jianxian Qiu, Dispersion and dissipation errors of two fully discrete discontinuous Galerkin methods, J. Sci. Comput. 55 (3) (2013) 552–574.
[49] D. Sarmany, M.A. Botchev, J.J.W. van der Vegt, Dispersion and dissipation error in high-order Runge-Kutta discontinuous Galerkin discretisations of the Maxwell equations, J. Sci. Comput. 33 (1) (2007) 47–74.
[50] Richard Courant, Kurt Friedrichs, Hans Lewy, Über die partiellen differenzengleichungen der mathematischen physik, Math. Ann. 100 (1) (1928) 32–74.
[51] S. Gottlieb, C.-W. Shu, E. Tadmor, Strong stability-preserving high-order time discretization methods, SIAM Rev. 43 (1) (2001) 89–112.
[52] A. Taube, M. Dumbser, C.-D. Munz, R. Schneider, A high-order discontinuous Galerkin method with time-accurate local time stepping for the Maxwell equations, Int. J. Numer. Model. 22 (1) (2009) 77–103.
[53] Shi Jin, Asymptotic preserving (AP) schemes for multiscale kinetic and hyperbolic equations: a review, in: Lecture Notes for Summer School on"Methods and Models of Kinetic Theory"(M&MKT), Porto Ercole (Grosseto, Italy), 2010, pp. 177–216.
[54] V. Vinduja, Trefftz-DG Methods and Tent-Pitcher Algorithm for Spacetime Integration of Wave Problems, PhD thesis, 2022.
[55] G.F. Carey, M. Tsai, Hyperbolic heat transfer with reflection, Numer. Heat Transf., Part A, Appl. 5 (3) (1982) 309–327.
[56] J. Palaniappan, S.T. Miller, R.B. Haber, Sub-cell shock capturing and spacetime discontinuity tracking for nonlinear conservation laws, Int. J. Numer. Methods Fluids 57 (9) (2008) 1115–1135.